Chapter 5

Simulated Performance of the Reference Design

The performance of the Auger Observatory reference design is evaluated using detailed Monte-Carlo simulations. The technical description of elements of the design will appear in later chapters. In this chapter, knowledge of the properties of air showers is applied to determine how data from the experiment will actually look and how it can be analyzed in order to achieve the stated goals of the Auger Project.

The MOCCA air shower simulation program is described first. This code is the basis for most of the predictions concerning the details of extensive air showers. Where possible, data obtained from previous observations of the highest energy cosmic rays by groups such as the Haverah Park, Akeno, and Fly's Eye Collaborations have been employed to verify the simulations.

Next, a description of the assumed parameters of the reference design is given, including both the surface and the air-fluorescence detectors. This is followed by a description of a total simulation program employing MOCCA, a detector simulation, and analysis algorithms, constructed to predict the performance of the surface array. The chapter concludes with a similar discussion of a simulation and analysis procedure for the Hybrid Detector, the integrated surface array and fluorescence detector system.

5.1 Numerical simulations

Numerical simulation of air showers is an essential tool for designing the detector and evaluating its performance. The simulation program needs to be efficient. All Auger Observatory showers produce at least 10^{10} particles. It is computationally prohibitive to simulate so many particles or to record simulated data for so many particles. A viable computer program must have an unbiased method for computing all relevant shower properties using a sampled subset of the full shower. The simulation program must also be accurate in modeling the relevant aspects of particle interactions. It must produce results which are consistent with those properties of giant air showers which have been measured.

As mentioned in the last chapter, almost all of the relevant physics is well established. Ambiguity in modeling the highest energy hadronic interactions has little impact on evaluating detector performance. The detector resolution concerns differences in measurable quantities (e.g. particle density from a 1.5×10^{19} eV shower vs. density from a 1.0×10^{19} eV shower, or X_{max} for an iron nucleus vs. X_{max} for a proton at the same energy). Such differences in measurable quantities have less model dependence than the quantities themselves.

We have elected to use principally the MOCCA program for the design of the Auger Observatory detectors. This program is described below. We then discuss some aspects of hadronic physics which are addressed by the interaction generator SIBYLL, which can be used within the MOCCA code. Following some comments on the ways in which the nucleus-nucleus interactions are treated, we highlight important verifications of MOCCA using air shower data.

5.1.1 The MOCCA Simulation Program

This program was created by A.M. Hillas for use with the Haverah Park experiment [126]. Variations have since been successfully used by many cosmic ray experiments studying events from 10^{12} eV to 10^{20} eV. The code performs both of the main functions required of an EAS simulation: the generation of the electromagnetic cascade through the atmosphere and the details of individual hadronic interactions and decays.

At the time MOCCA was created, the speed of computers was very slow by today's standards. This program employs novel and efficient methods for generating and following the many particles in large air showers.

Particle production in hadronic collisions is simulated using a splitting technique [127]. The center-of-mass energy in the collision is apportioned between a leading particle and the production of new particles. The energy assigned to new particles is subdivided into four parts. Each part is further split in two, one of which is assigned to a single pion. The process is iterated on the unassigned energy packets until all the energy of the initial interaction is exhausted. The leading nucleon and newly produced pions are tracked until they interact again or decay, as appropriate.

This algorithm produces a spectrum of produced particles in accord with data from fixed-target accelerator experiments. This results both from the nature of the algorithm as well as *a priori* assumptions (e.g., cross sections). Specific features arising naturally from the method[127] include a flat Feynman-x distribution of the leading nucleon, Feynman scaling of resulting momentum distributions, KNO-like charged particle multiplicity distributions whose mean values increase with energy as ln(s), constant mean transverse momentum, and momentum and energy conservation.

All newly produced particles are assumed to be pions. In reality, roughly 10% of these particles would be kaons. This does not seriously alter the resulting muons, electrons, and photons of the air shower, since the interactions and decays of pions and kaons are similar.

Variations can be made in the algorithm to alter the probability distributions in the assignment of pion energies. Such changes can affect the inelasticity of the interaction and consequently the kinematics of the produced particles. The effect on air shower particles at the ground is not enormous, but it can be measurable. The effects of different variants of MOCCA are described below (cf. Figure 5.2).

It is not computationally possible to follow all the particles in an air shower. MOCCA uses a technique called "thinned sampling" to track semi-randomly selected particles. Those arriving at the ground have associated weights to indicate how many others were neglected in the procedure. For the 10^{19} eV showers used in this work, the weights may be as large as 10^5or 10^6. The method allows accurate computation of the total energy arriving at the ground and shower size (i.e. the total number of particles at the ground), but the study of fluctuations requires special care.

5.1.2 The SIBYLL Interaction Generator

As mentioned above, the MOCCA program uses an algorithm to generate the details of hadronic interactions which yields results that match fixed-target accelerator experiments. Certain new aspects of particle production became apparent with the advent of higher energy accelerators such as the CERN proton-antiproton Collider. SIBYLL is a hadron interaction simulator which was developed to address these developments.

SIBYLL is described fully elsewhere [128]. Pertinent to the design of EAS detectors are the following features. Hadron interactions are modeled with parton strings, similar to the algorithms in the Lund Monte Carlo extensively used in analysis of accelerator experiments. The multiplicity increases more quickly (as $ln^2(s)$) than at lower energy and exhibits violations of the KNO distribution. The proton-proton cross section increases more quickly with energy, there are correlations of transverse momentum with multiplicity, and there is the onset of a "hard part" of the cross section ("minijets").

These new features of particle production and kinematics match data from the CERN Collider. The onset of these features is made smoothly as the collision energy increases. Thus, SIBYLL produces hadronic interactions which are quite similar to those of MOCCA even when the particle energy approaches 100 TeV. The algorithms differ more as the energy increases. The number of pions produced in an air shower is not substantially different from what would be obtained from MOCCA in its basic form. The main effect of SIBYLL arises from the scaling violations which soften the energy distribution of pions and so ultimately alter the number of muons in the cascade.

SIBYLL can be used within MOCCA instead of the usual algorithm. The difference between the two approaches will occur mainly in the earliest interactions in the showers, after which the energies are reduced to levels where the algorithms give similar results. Figure 5.1 exhibits the distribution of the energies of hadron collisions in proton air showers. Only a small fraction of these occur in regimes where SIBYLL and basic-MOCCA differ significantly.

We thus can expect that features of air showers which do not depend on the first

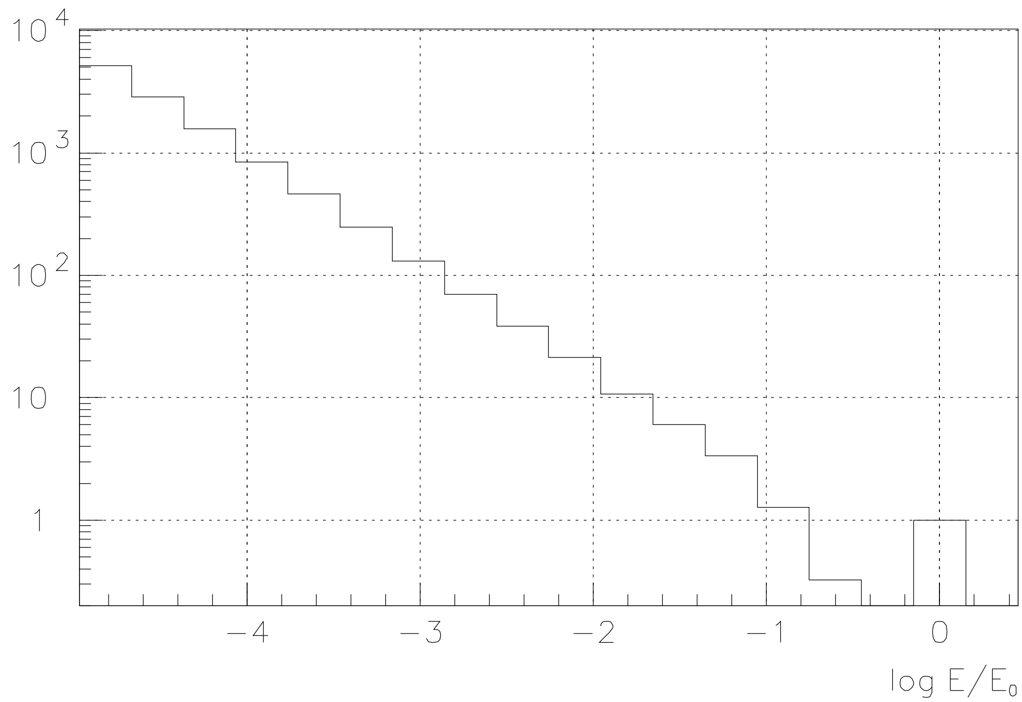

Figure 5.1: The distribution of interaction energies of hadron collisions in proton air showers, expressed as a fraction of the primary cosmic ray energy. This plot shows the highest energies of the distribution, obtained from an average of 100 showers at 10^{17} eV.

few interactions in the cascade will be relatively insensitive to whether the basic MOCCA algorithms or the more sophisticated SIBYLL approach are used. The depth of maximum of the shower is an example of a quantity which does depend on the location and features of the first interaction. X_{max} has been shown to be rather different when SIBYLL is employed. On the other hand, the total number of charged particles at the ground is not greatly changed. The number of muons at ground level shows somewhat more sensitivity to the choice of hadron interaction algorithm. (Ground particle differences are discussed further in Sec. 5.1.4 below.)

Finally, it must be considered that there is uncertainty in extrapolating the dynamics of particle interactions to the highest energies. The predictions of the MOCCA program, with or without SIBYLL, will be affected by the choice of extrapolation. Some interesting propositions can probably be tested by analysis of the structure of air showers. But it must also be stressed that only a limited set of basic shower characteristics are necessary to properly design a detector to achieve the stated goals of the Auger Project. These characteristics, such as the lateral distribution of particles and the timing structure of the shower front, derive mainly from the lower energy interactions in the shower. They are not greatly affected by reasonable alternative physics assumptions [84]. This, and the demonstrated good agreement with existing data (discussed below), leads us to conclude that the features of air showers most critical to the design of the detector can be confidently predicted using

MOCCA.

5.1.3 Nucleus-Nucleus Interactions

It is more difficult to construct algorithms which simulate the details of nucleus-nucleus collisions than it is to model proton-nucleus interactions. A simple approximation which is often used is the *superposition model.* In this approach, the interaction of a primary nucleus with A constituent nucleons and total energy E is modeled as A independent single nucleon collisions, each with energy E/A.

It has been rigorously shown [129] that this approximation will correctly produce the average values of "additive" quantities in air showers such as the total muon or electron numbers at the ground. The fluctuations in these same quantities will however be underestimated. Note that the depth of shower maximum is not an "additive" quantity in an atmospheric cascade.

The dynamical modelling of MOCCA in Auger Observatory simulations is more realistic than that of the simple superposition model. Firstly, it is to be emphasized that the SIBYLL interaction code simulates hadron interactions only. SIBYLL, whether employed in MOCCA or in the context of other air shower programs, is usually augmented with auxiliary code which generates features of nucleus-nucleus interactions in a somewhat more sophisticated manner than the simple superposition model. The fragmentation of nuclei during collisions and the cross sections of nuclei-on-nuclei are modeled after accelerator data. The interaction is thus reduced to a set of individual nucleon-air collisions which are simulated by SIBYLL.

5.1.4 Comparison to Data

The MOCCA simulation reproduces many characteristics of air showers measured by ground arrays. One very important feature of EAS is the lateral distribution of particles. Figure 5.2 shows the results of the simulation compared to data from the AGASA experiment. While the reference design of the Auger Observatory differs significantly from the hardware of the AGASA array, comparisons between the simulation and this experiment are more direct. Results of detector simulations using MOCCA air showers and the Auger Observatory reference design detector were shown in the last chapter and more will be discussed in the next.

Figure 5.2 shows several separate simulations done with MOCCA under a variety of assumptions. Results for three variants of the code are shown. One is the original MOCCA algorithm. Another is a more recent version of the code called "MOCCA92" which incorporates some slight changes in: pion transverse momentum distributions (harder), proton-air collisions elasticity (more elastic), and multiplicity of some interactions (higher). Finally, a variant using MOCCA92 and the SIBYLL interaction generator is shown, which also employs some small updates in various secondary hadron cross sections. All three simulations were done using 10^{19} eV oxygen nuclei as the primary cosmic rays in order to account for

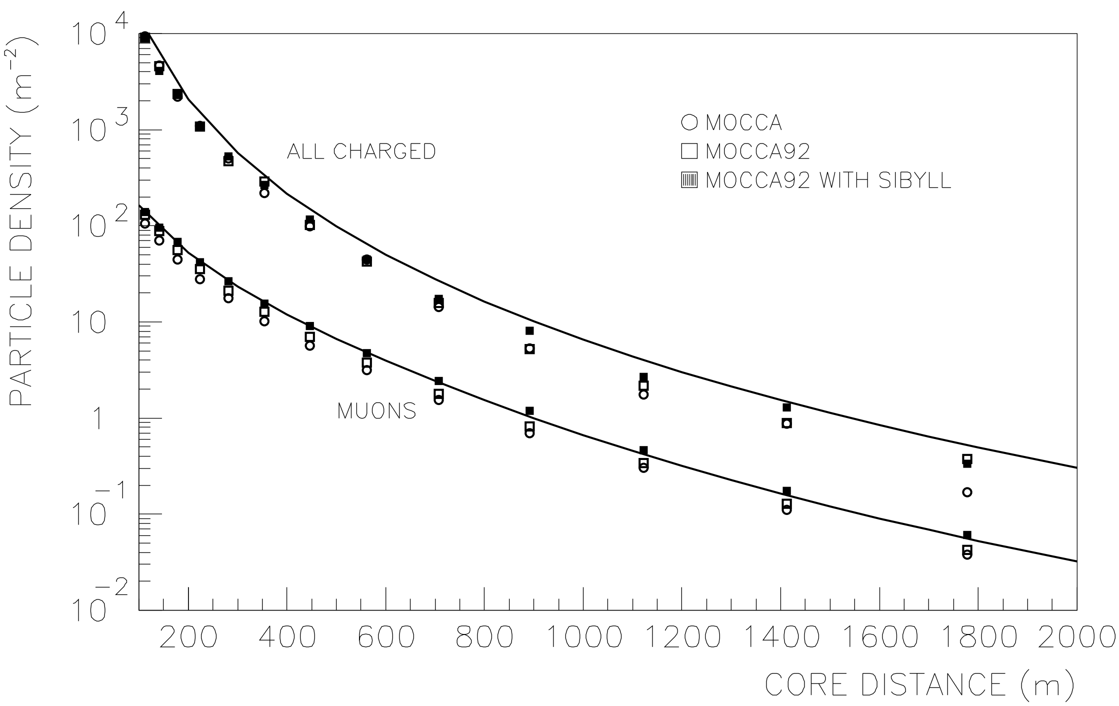

Figure 5.2: Lateral distributions of electrons and of muons from MOCCA simulations of 10^{19}eV oxygen showers. Three different interaction models are indicated: original MOCCA, the modified MOCCA92, and MOCCA92 with the SIBYLL interaction generator. Points are simulations, solid lines are published fits of the Akeno data. The upper curve and points are all charged particles, the lower for muons only.

the fact that the cosmic rays seen by Akeno are probably neither purely protons nor purely iron. While differences are evident, there is generally good agreement between data and simulation, especially for the muons.

The MOCCA92-SIBYLL version best matches the muon lateral distribution data. The different physics assumptions inherent to the three variants of the code result in systematic differences of as much as 60% in the muon densities. Given that the density itself varies over more than 5 orders of magnitude over the lateral range examined, such differences do not seriously alter the design of the array. These differing results should be interpreted as indicating the degree to which "reasonable" variations of the physics assumptions affect the predictions of the simulation programs.

The arrival time of particles at the ground is another aspect of air showers of great importance in the technical design of a detector. The shower front has a roughly conical shape. The MOCCA prediction for the delay times of particles (relative to a planar shower front) as a function of core distance is given in Figure 5.3. Also shown is a parametrization of this quantity obtained from fits to the Akeno data [130]. There is excellent agreement between the simulation and the data from 30 m to 3 km from the core (The Akeno fit is not intended to be valid at closer core distances). Similar good agreement is found when

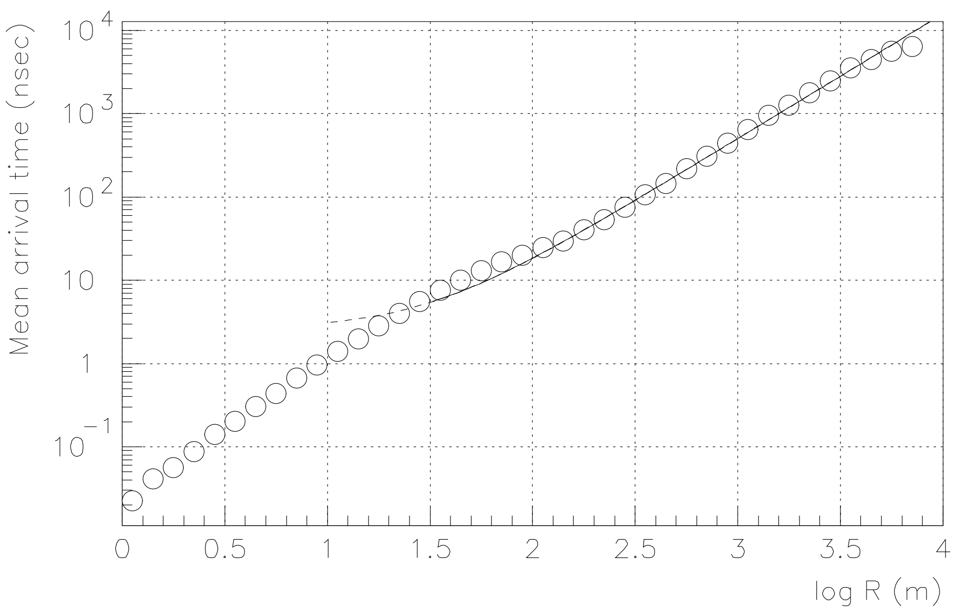

Figure 5.3: Mean arrival time of charged particles with respect to those at the core, from MOCCA simulations of 10^{19} eV proton showers. The solid line is a published fit of Akeno data.

comparing the r.m.s. spread in arrival times between MOCCA and the Akeno data.

Having confidence in the ability of MOCCA to properly represent the time structure of the shower front, we use the results of the simulation to guide the design of the detector electronics. Figure 5.4 gives information from MOCCA on the thickness of the shower front. It can be seen that particles will be arriving over a span of several μs, with the muons arriving earliest. As a more extreme example, MOCCA predicts that a 20 μs wide window contains virtually all the particles in the shower front of a 10^{21} eV event at 3.5 km from its core. The majority of the data will be at a lower primary energy and the particles will span a smaller time interval (see Fig. 5.13 in Sec. 5.2.4 below).

5.1.5 Ongoing studies

Many of the most important features of air showers relevant to the design of the Auger Observatory are insensitive to all but the most extreme variations of the details of the interaction models used in the simulations. For example, while the multiplicity of charged particles produced in hadron interactions is uncertain at the highest energies, the shower size at the ground has been found to be unchanged by "reasonable" extrapolations of lower energy data. Characteristics of the muons at ground level do show possibly measurable effects, as discussed previously, but in most cases not of a sufficient magnitude to seriously alter the conclusions arising from the simulation studies described here.

Similarly, aspects of air showers relevant to air fluorescence detection, such as X_{max},

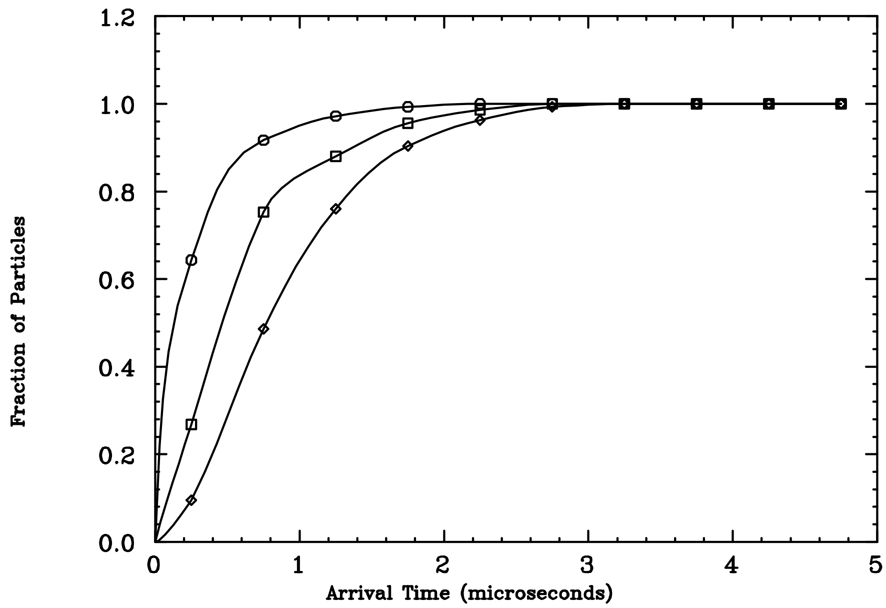

Figure 5.4: Integrated arrival times of charged particles with respect to those at the core, from MOCCA simulations of 10^{19} eV proton showers, sampled 900 m from the core. The three curves indicate respectively the muons, photons, and electrons. The muons arrive the earliest. Solid lines are to guide the eye.

have also been studied to examine their behavior under different physics scenarios [84]. Except under very extreme models, the design of the detector is not affected by such changes.

An ongoing program has been organized to compare different simulation codes, to produce more efficient drivers, and to develop the most realistic interaction models.

5.2 Surface Detector Simulation

This section describes how the ground array is expected to function and fulfill the triggering and performance requirements set forth in earlier chapters. First, we describe some elements of the Auger Observatory reference design used in the simulations which follow. Then, a summary is given of air shower characteristics which are important for our design. Next, a detailed simulation of the water Čerenkov tank system is given with attention paid to how the simulations are checked against earlier data. Finally, simulations are used to gauge the ability of the analysis algorithms to reconstruct the energy, direction, and composition of cosmic rays.

Calculations of the performance of a Hybrid detector (a surface array and fluorescence detectors as an integrated device) have been done independently of the simulations of the reference design surface array by itself. This work is given in a later separate section.

5.2.1 Detector description

Water Čerenkov detectors have been selected as the technology for the Auger Observatory surface array. This device consists of a volume of clear water acting as a Čerenkov radiator viewed by one or more photomultipliers. We have assumed a cylindrical detector 1.2 m deep with a top surface area of 10 m^2 (a radius of 1.8 m). The depth is a nominal value which allows a direct comparison with the existing experimental data from Haverah Park. We comment later (Section 5.2.5) on how a deeper tank may be useful for muon identification.

The volume of water is viewed from above by three large (200 mm diameter) photomultiplier tubes. The PMTs are placed at 120° intervals on a circle of radius 1.2 m (2/3 of the detector radius), looking downward from the top surface of the tank. The inner walls of the tank have a diffusively reflective white surface. The detectors are assumed to be arranged on a triangular grid with 1.5 km spacing between each station and its nearest neighbors.

5.2.2 Air Shower Structure

The performance of the detectors is sensitive to the detailed characteristics of the air shower particles. Before considering the details of a detector simulation, the air showers themselves are examined. The MOCCA simulation program which was described in the last section is used for this purpose. Good agreement was shown between the simulation and data from the Akeno experiment, demonstrating that MOCCA gives reliable predictions of air shower particles prior to their entering the detectors.

Features of the energy and arrival times of particles in the shower front are presented first, followed by discussion of the observable differences between showers initiated by protons and those from iron nuclei.

Particles in the shower front

A water Čerenkov tank differs significantly from other types of detectors (e.g. plastic scintillator or RPCs) in the way it responds to air shower particles. This kind of device will be relatively more sensitive to muons. To understand why, it is necessary to consider detailed features of the particles.

At ground level, far from the core of an EAS, the shower front consists of gammas, electrons and muons. There is also a flux of (evaporation) neutrons which are generally sub-relativistic and so are delayed with respect to the main shower front, and large numbers of atmospheric Čerenkov photons. The relativistic hadron flux is negligible beyond 50 m from the core.

The muons and electromagnetic particles have very different energies. The distributions shown in Figure 5.5 were obtained from MOCCA simulations of vertical 10^{19} eV proton showers, sampled 900 m from the shower core. A typical muon has an energy of about 1 GeV, while the majority of electrons and gammas are below 10 MeV. Note that electromagnetic

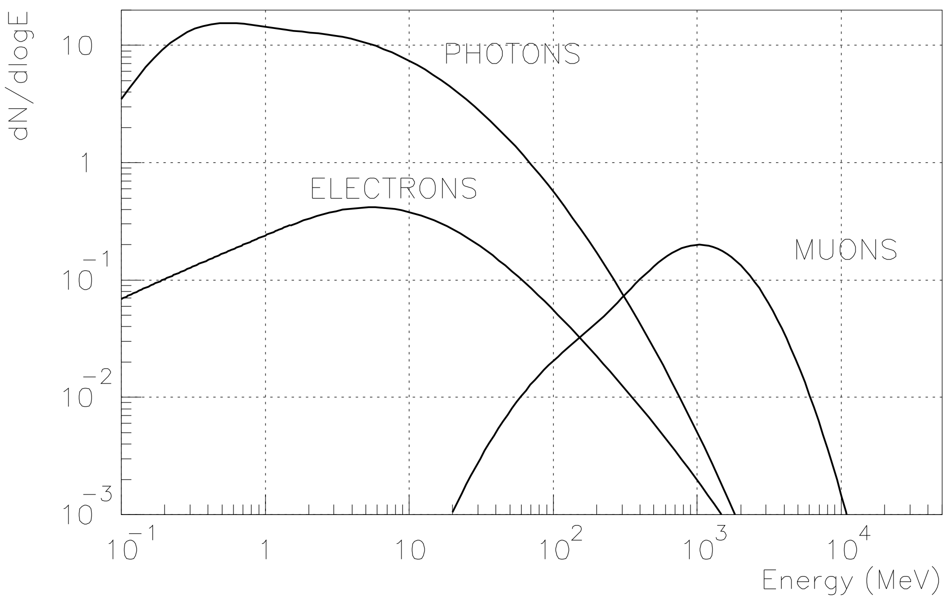

Figure 5.5: Distribution of particle kinetic energies at the ground for 10^{19} eV proton air showers, from MOCCA simulations. Ground level is taken to be 1000 g/cm^2 and particles are sampled at a core distance of 900 m.

particles greatly outnumber muons within a few kilometers of the core.

As a consequence of their higher energies (and masses), air shower muons travel much further than electrons in water. Thus, they produce a great deal more Čerenkov light in the tank. Despite their relatively small contribution to the total number of particles at the ground, muons can dominate the signals obtained from water Čerenkov detectors (recall Figure 4.2.

Figure 5.6 shows the correlation between the energy, density, and arrival times of different particle types from a set of simulated showers with the same properties as in the previous figure. Electromagnetic particles suffer significant scattering and energy loss during the course of the shower, resulting in effective "path lengths" to the ground much longer than straight line trajectories from the shower axis. Thus muons, in addition to having higher energies, also arrive earlier and over a much shorter period of time than the electromagnetic particles. These features help distinguish muons from electrons and photons, which will be useful in the study of cosmic ray composition. This is described next.

Shower features related to primary type

Muons in air showers are expected to show particular sensitivity to the nature of the primary particle. Showers initiated by iron nuclei have significantly more muons than do proton induced showers of the same energy. It is therefore useful to carefully consider the properties of air shower muons which will be relevant to their detection. The predicted numerical

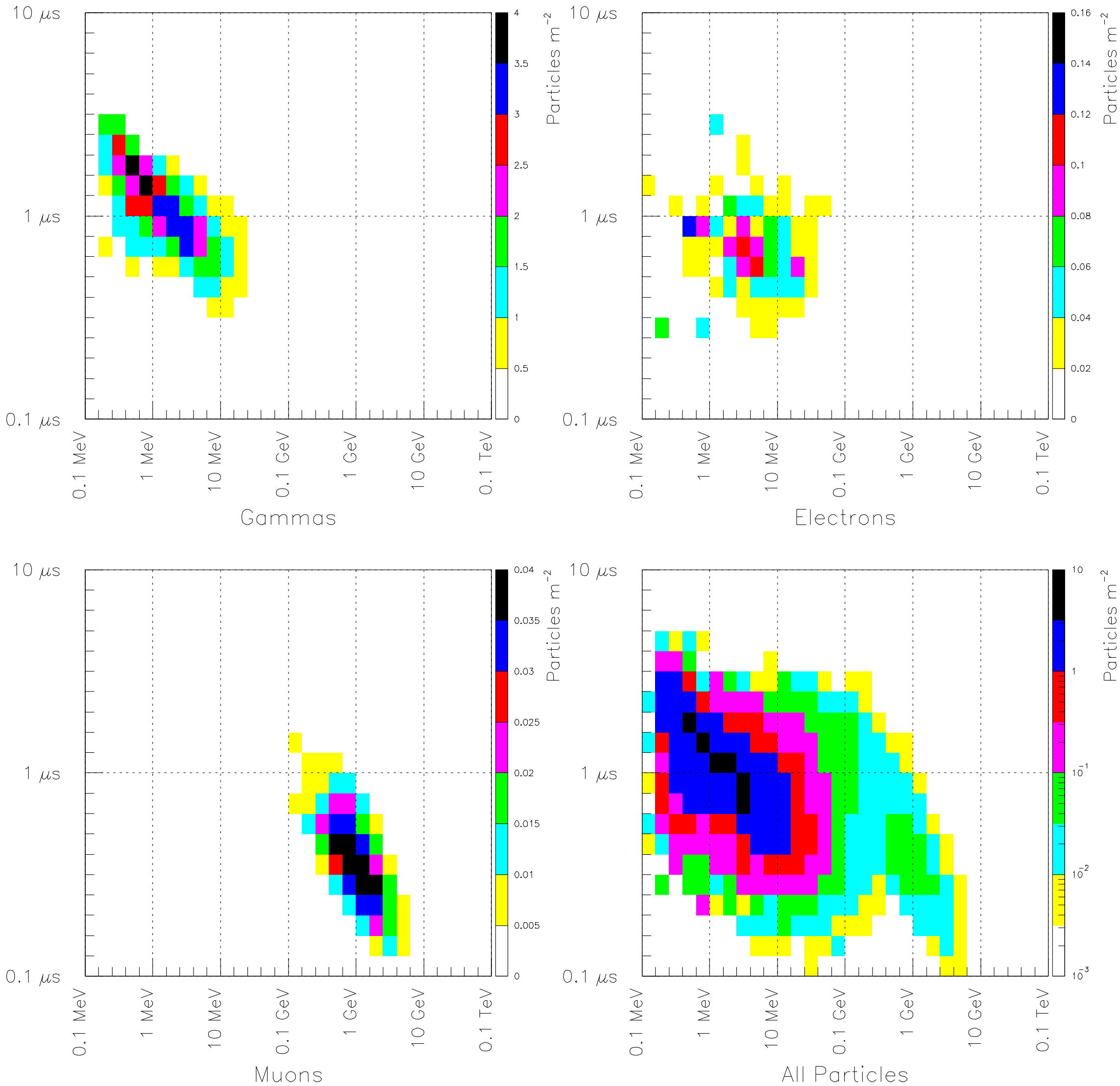

Figure 5.6: Correlations between energy, arrival time, and density for shower particles at 900 m from the core of a vertical 10^{19} eV proton initiated EAS, from a set of MOCCA simulated showers. Observation level was taken to be 1000 g/cm^2 atmospheric depth (near sea level). Note that the density scale for the all particles plot is logarithmic to allow the muons to be seen on the same scale as the electromagnetic particles.

densities of muons, electrons, and photons at sea level in 10^{19} eV proton- and iron-initiated air showers are shown in Figures 5.7(a) and 5.7(b).

At ground level the differences (other than the total number of muons) between iron and proton showers are relatively small; Figure 5.7c shows the predicted numerical density ratio of the shower component particles for iron and proton showers. The electromagnetic densities are similar, but there are $\geq 75\%$ more muons in the iron showers at the core distances of interest (≥ 1 km). Although the absolute number of muons for a shower of given energy and primary type is somewhat dependent on the details of the hadronic interaction model, the *ratio* of the densities of proton and iron showers is much less model dependent.

The amount of Čerenkov light generated per muon is very different than the amount generated per electron. In 1.2 m depth of water a large fraction of the muons will "punch through" the detector volume. However, the majority ($\geq 90\%$) of the electromagnetic energy will be absorbed (the mean free path of gammas in water is $\leq$ 0.5 m). Additionally, Čerenkov light yield is only proportional to energy loss for particles which are fully relativistic, which is not true for much of the total electromagnetic track length. For these reasons interpretation of the light yield recorded by a water Čerenkov array must rely on comparison with shower and detector simulations to ultimately determine the shower energy. (In fact all EAS detectors are dependent on shower and detector modeling for event energy reconstruction). Roughly speaking, the water Čerenkov signal density is proportional to the sum of muon *number* density (multiplied by the average muon energy loss) and the electromagnetic *energy* density.

Earlier (section 4.2.3), the ratio of muons when compared to electromagnetic particles was shown to be useful in the study the primary composition. Determining the fraction of the signal due to muons on the basis of pulse height will only be practical at large core distances where the density of electromagnetic particles is not so high as to overwhelm the muon signals. In a 5×10^{19} eV shower there will be ~ 5 detectors in the core distance range where the particle density is appropriate. Figure 5.7d shows the predicted proportion of electromagnetic "fake muons" – electrons or photons whose signal has fluctuated upward so as to resemble that typically expected from a muon. At core distances ≥ 1 km this fraction is $\leq 10\%$. The potential for accurately determining the fraction of muons among all the particles striking a detector is also dependent upon the proportionality of the detector response: the signal from each particle must be closely proportional to the Čerenkov light released.

5.2.3 Detector Simulation

A simple but very fast Monte Carlo simulation of the response of a cylindrical water Čerenkov detector to incident gamma, electron and muon particles has been written. Air shower particles from the MOCCA program are passed to this simulation to assess the response of the surface array. This section gives the assumptions used to model physical processes in the detector, the methodology of the procedure, and finally the results and analysis of the simulated air shower events.

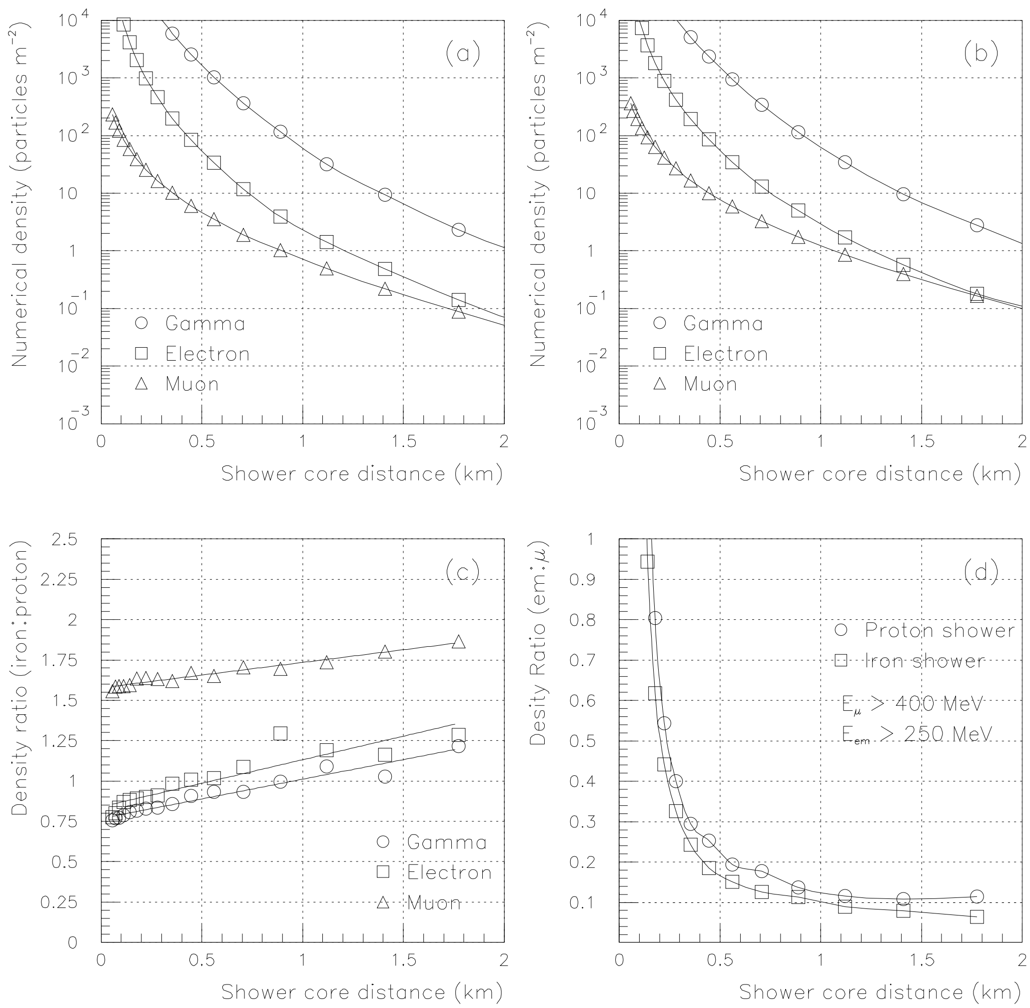

Figure 5.7: Predictions of shower front characteristics from the MOCCA EAS simulation program, without detector simulation. (a) shows the lateral distribution of an average vertical 10^{19} eV proton shower; (b) is identical but shows an average iron shower. Atmospheric depth is 1000 g/cm^2; (c) shows the ratio of (b) to (a) as a way of comparing properties of proton and iron showers at this energy; (d) is the number of electromagnetic particles which will produce a burst of Čerenkov light in a 1.2 m deep detector equal to that from a penetrating muon, shown as a fraction of the number of penetrating muons.

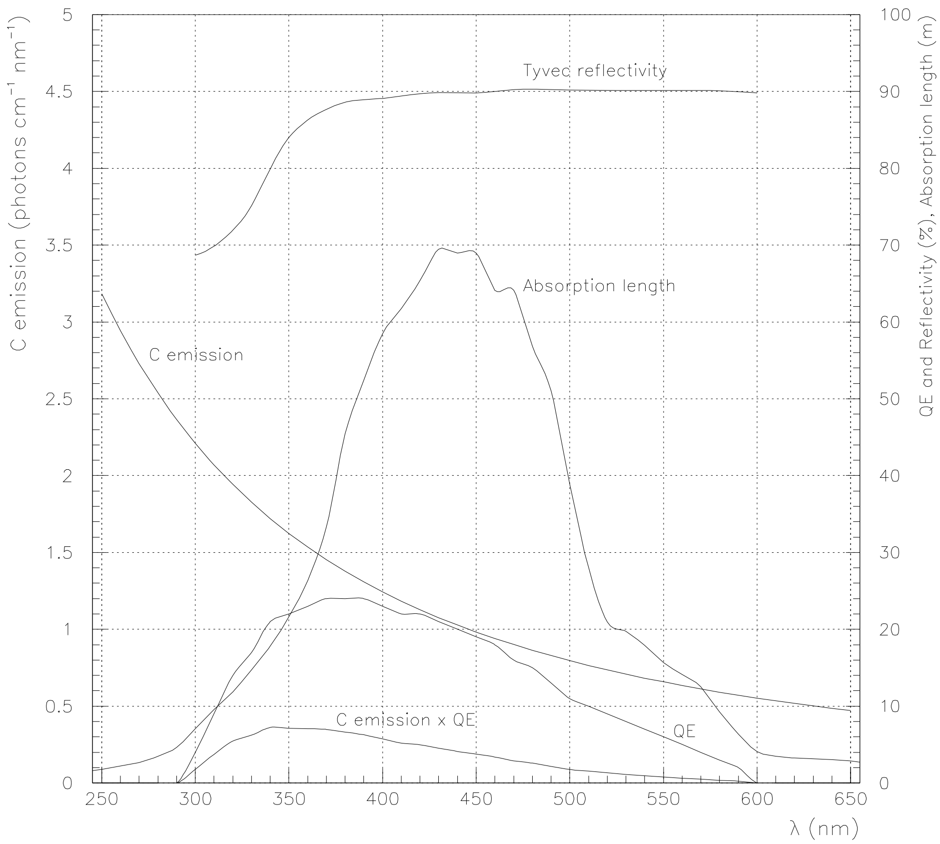

Figure 5.8: Some important spectral characteristics for a water Čerenkov detector. The quantum efficiency shown is for a bi-alkali photocathode. Absorption length is for ultra-pure water. Tyvec is a plastic material which may be used as a lining for the tank; see Chapter 7 for further details.

Čerenkov Radiation

Čerenkov light is produced by a charged particle moving through a transparent medium with velocity $\beta \geq 1/n$, where n is the refractive index ($n = 1.33$ for water). Hence a particle must have a kinetic energy greater than half its rest mass energy to radiate Čerenkov light (0.25 MeV for electrons and 73 MeV for muons). The angle of emission is $\theta = \cos^{-1}(1/\beta n)$ with respect to the particle trajectory: 41° for a fully relativistic particle in water.

The yield of Čerenkov photons with wavelengths between λ_1 and λ_2 for a small element of particle track dx is given by:

$$\frac{dN}{dx} = 2\pi\alpha\left(\frac{1}{\lambda_1} - \frac{1}{\lambda_2}\right)\left(1 - \frac{1}{\beta^2 n^2}\right),$$

where α is the fine structure constant. Figure 5.8 shows the Čerenkov emission spectrum for water calculated on the basis of the above equation.

Material Characteristics

The choices of the various elements of the reference design surface detector are described in detail in the next chapter. Reviewed here are some elements which are especially pertinent to the simulation.

In Figure 5.8 photomultiplier quantum efficiency[1] is shown as a function of photon wavelength. The convolution of quantum efficiency and the Čerenkov emission is also shown. Clearly the wavelength region between 300 and 500 nm is crucially important. The spectral diffuse reflectivity of a material called Tyvec[2], a possible interior lining material of the detector tank, is shown. Finally the absorption length of pure natural water is shown[3], and is seen to exceed 10 m across the wavelength range of interest.

The spectral characteristics of the scattering (Mie scattering) and absorption of light in water containing particulate impurities are functions of the numerical density, size spectrum, and composition of the impurity particles. Values below the ultra-pure curve shown in Figure 5.8 are expected for water whose quality is practical for this application. Behavior varies greatly depending on the source and purification processing of a particular water sample. See Chapter 7 for further discussion, and some preliminary measurements.

The complexity of the spectral dependence of the net absorption length of water requires that it be measured specifically for any samples of water used in a detector. So details such as assigning each Čerenkov photon a wavelength sampled from the emission spectrum have not so far been explicitly included in the simulations. Instead (and also to speed up the simulation process) the number of Čerenkov photons emitted for each particle track increment is set equal to the integral of the convolution of the emission and detection characteristics. Fixed water absorption length and lining material reflectivity are assumed. The validity of this approximation depends upon the extent to which these values vary over the spectral range of interest (300 to 500 nm) in combination with the size and geometry of the detector. Further work on this point is in progress.

Other approximations regarding the physical parameters of materials have been made for the purposes of simulation. The numbers used represent average or effective values over the range 300 to 500 nm, and are believed to be realistically achievable. Here, a summary of the numerical values used in the simulation:

- 15% photocathode quantum efficiency;
- 85% reflectivity of the tank lining material;
- 7 m water absorption length;

[1] Taken from the Hamamatsu R1408 data sheet. This is a hemispherical PMT 200 mm in diameter in a borosilicate glass envelope which was used in the IMB experiment.

[2] The curve shown is for light incident at 30° to the normal, but there is little angular dependence. Measurements made by Surface Optics Corp. for UCI School of Physical Sciences.

[3] Taken from a 1981 review of the available data[131]

- 10% : 90% split between perfectly specular and perfectly diffuse reflection behaviour for photons reflected from the lining material. (It turns out that the split ratio assumed has little effect on the results).

It is to be emphasized that to a very good approximation the assumed parameter values affect only the absolute photoelectron yield for a given incident particle. They do not affect the validity of the comparisons with experimental data discussed in Section 5.2.4 below, where simulated detector calibration has been carried out.

Detector Simulation Algorithm

The full simulation of the response of the Auger Observatory surface detector array has three distinct elements: production of air shower particles using MOCCA, calculation of the detailed response of the water Čerenkov detectors and electronics, and the construction of realistic event triggering.

The MOCCA program was described above. Recall that an important aspect of this code is the *thinning* of the shower in order to keep the computation time manageable. Only a very small fraction of the total number of air shower particles, each with a large weighting factor, are provided by the simulation. The number of particles provided is very small at core distances ($>$ 1 km) typical of events in the array.

To remove such artificial fluctuations due to small numbers, individual MOCCA showers are not used to create individual events. Rather, sets of showers are run under fixed conditions, the weights summed , and then averages are taken. This has the unfortunate effect of also averaging out the physical fluctuations due to variations in the atmospheric depth of the first interaction point and shower development. (Note that a different simulation procedure will be employed in simulations of the so-called Hybrid system, a combined surface array - optical detector described later).

Batches of 100 showers have been generated for proton and iron nuclei primaries at 0°, 30°, 45° and 60° zenith angles. All the simulations are for primary energy of 1×10^{19} eV and an atmospheric depth at ground level of 1000 g/cm^2. The energy threshold at which particle thinning commenced was 10^{-6} of the primary energy (10 TeV).

The generation of simulated experimental data is then done in the following steps:

- Output from the averaged MOCCA showers is in the form of a ground particle list giving particle type, impact coordinates, trajectory, thinning weight, and energy. Each particle is projected onto the plane perpendicular to the shower axis passing through the core impact point and then binned into a 5-dimensional array to give differential energy/time/density breakdowns for each particle type at given core distance. (Figure 5.6 was an example of the information in the annular bin centered at 0.9 km from shower core). It is not practical to further subdivide the ground particles into other categories (e.g., their trajectory angle) because of the limited computational statistics.

- To generate individual showers for a particular primary type and zenith angle a random azimuthal angle and core impact position are selected and a shower projected onto the simulated array grid. For each detector the core distance in the shower plane is calculated and the pre-determined density array re-sampled to generate a list of shower particles striking that detector, each particle being assigned impact coordinates, an energy, and an arrival time. By sampling over an area in the plane of the detector top surface (but larger), all "corner clipping" effects are automatically included.

- The detector simulation program is invoked using the lists of particles striking the detectors. Each particle is tracked through the detector volume, interacting and radiating Čerenkov light. The resulting photons are ray-traced until absorbed in the water, upon reflection, or at a PMT. A list of photoelectron release times is updated for each detector.

- The photoelectron lists are used to construct simulated amplitude versus time profiles for the summed signal from all tubes. Care is taken to represent the effects of the electronics. This profile is then scanned and an *alert* condition is imposed to simulate the lowest level (hardware) trigger of an individual detector station. A GPS event time stamp is generated which reflects the fluctuations of the trigger time relative to the shower plane arrival.

The simulation of the Čerenkov photons in the detector is illustrated in Figure 5.9. Here, the propagation of the individual photons from a single penetrating muon is shown. All the particles in the air shower which strike detectors are simulated in this manner.

Figure 5.10 shows the final output of the simulation process for a single shower. The data thus generated is then available for event reconstruction and comparison with experimental data. Note that because the shower input data from MOCCA has already been averaged, intrinsic shower-to-shower fluctuations will not be reproduced. However, all detector imposed limitations due to limited size, non-proportionality, etc., are modeled in this procedure.

Note also in the lower part of Figure 5.10 that muons give large, narrow pulses. The more numerous electrons and converted gammas tend to yield smaller pulses individually, but these overlap and add together giving a broad baseline pulse, especially near the core. The ability to distinguish muons by their signal characteristics is one component of methods to evaluate the nature of the primary particle causing the air shower.

5.2.4 Comparison of Simulation and Data

To check the validity of the shower and detector simulations, their predictions have been compared to experimental results from the Haverah Park array. Since the reconstruction of the lateral distribution of particles is central to all analyses from the surface array, substantial attention is devoted to this topic here. It will be shown that the simulation reproduces many details of the data.

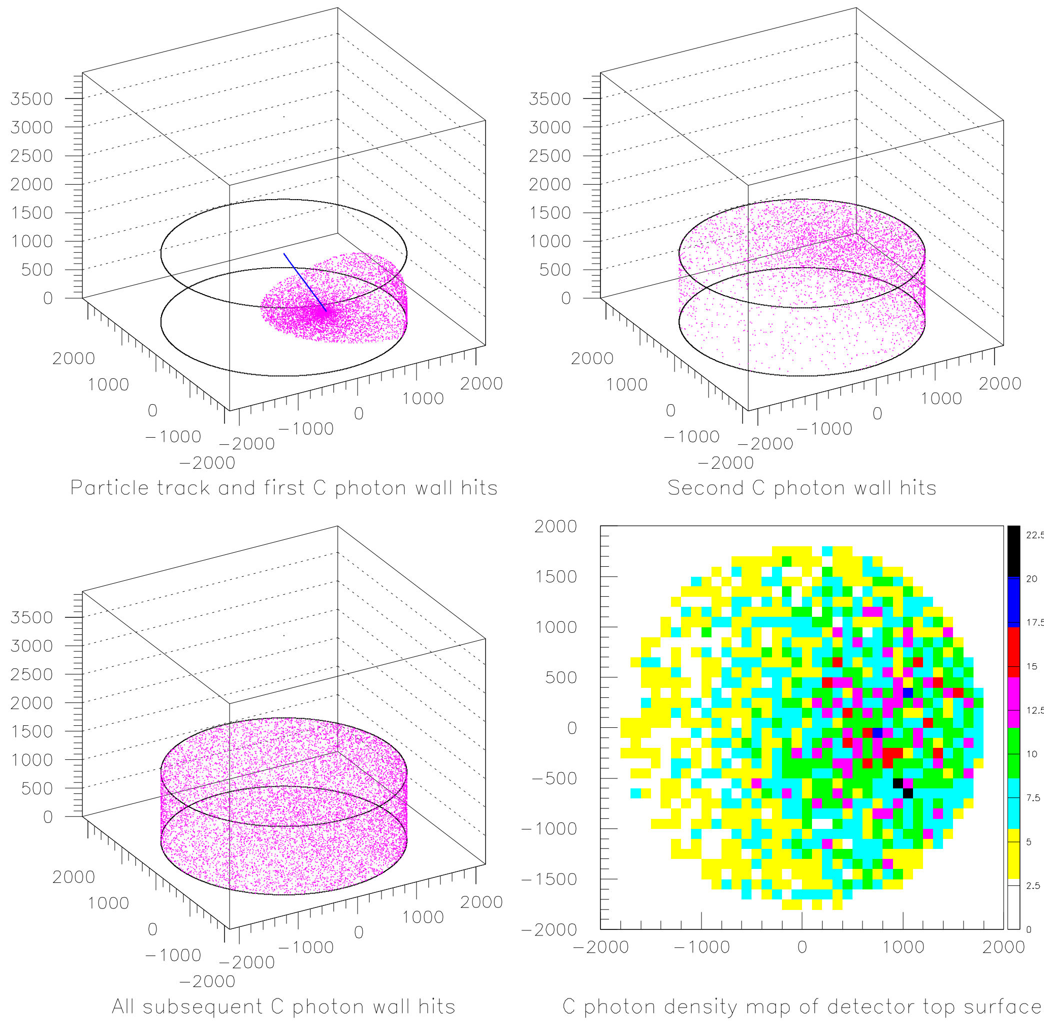

Figure 5.9: Simulation display for the reference design water Čerenkov detector unit. A single 1 GeV muon was injected at the center of the top surface traveling at 30° to the vertical. The upper left plot shows the incident particle track and the positions where the Čerenkov photons released first reflect from the tank walls. The upper right plot shows the positions of the second photon reflections. Reflections continue until the photons have been absorbed in the water or by the tank lining material; all reflection positions after the second are shown in the lower left plot. The distribution of reflection positions over the detector top surface integrated over all reflections is quite uniform. At lower right a density map of the detector top surface is shown.

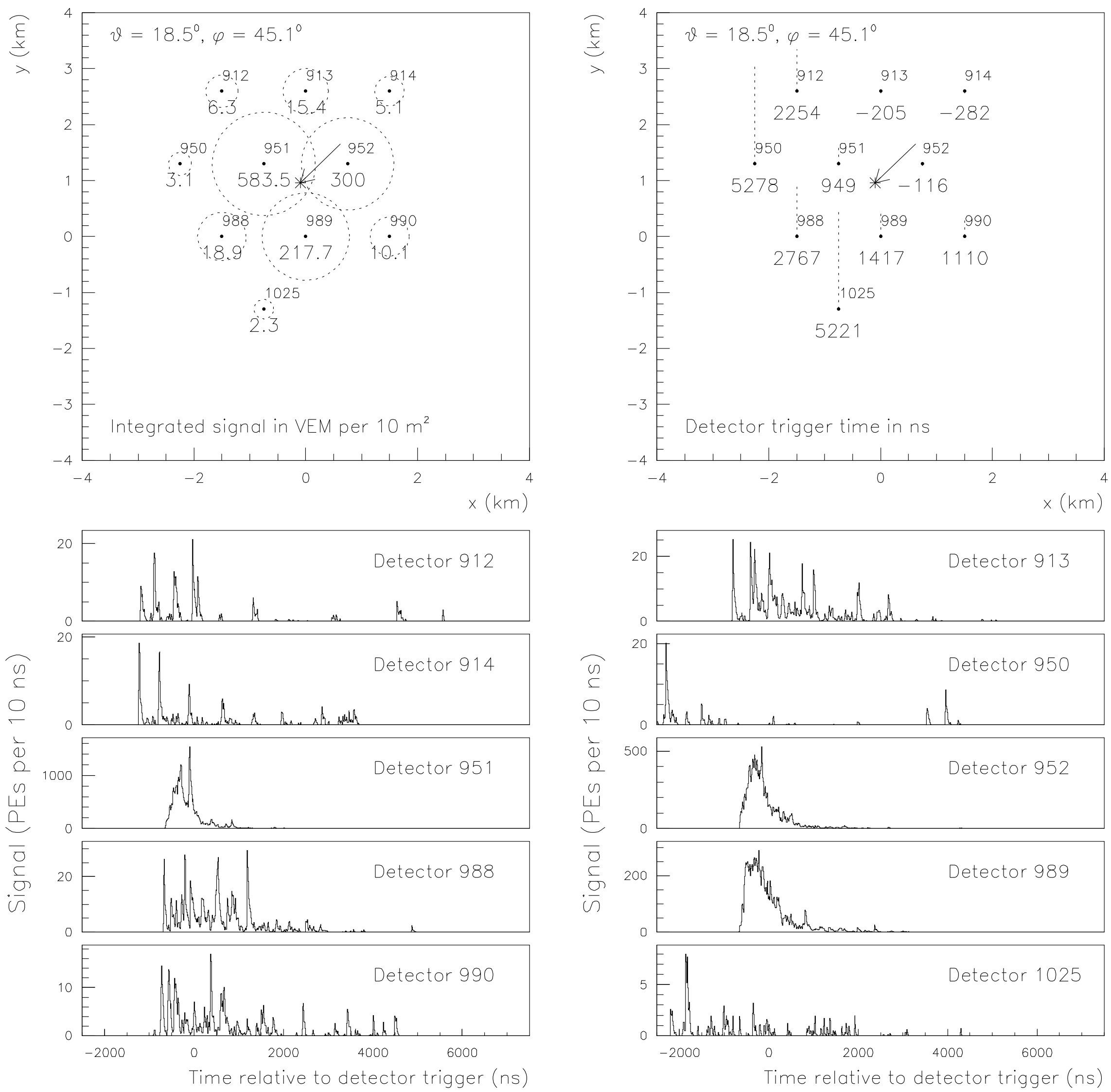

Figure 5.10: Illustration of a simulated EAS event falling on the reference design Auger Observatory water Čerenkov surface array. The shower was initiated by a 6×10^{19} eV iron nucleus incident at a zenith angle of 19°. The top left plot shows a ground plane signal density map, the radius of the circles being proportional to the logarithm of the time integrated signal. At top right is a map showing detector trigger times, the length of the vertical lines indicating the time relative to shower core impact. The lower part of the plot gives the time/amplitude signal profiles for each triggered detector — note the differing vertical scales.

Sets of showers have been run for various primary types and zenith angles using the procedures described above. Each of the Monte Carlo data sets presented in this section is the product of such a run. Event reconstruction errors have not been included at this point, the exact core distance being used to analyze the simulated measurement of particle lateral distributions. Note that one should not expect perfect agreement between the simulated events and the Haverah Park data since the simulated detector unit is not the same size and shape as the Haverah Park units. However, for the present case these effects will contribute second order discrepancies only.

Lateral distribution shape

In the last chapter (section 4.3.1), the lateral distribution function observed by the Haverah Park experiment was described. To review, a good fit to that data was empirically found to be a modified power law function:

$$\rho(r) = kr^{-\left(\eta+\frac{r}{4000}\right)}, \tag{5.1}$$

where shower core distance r is in meters, k is a normalization parameter, and η is given by

$$\eta = 3.49 - 1.29\sec\theta + 0.165\log\left(\frac{E}{10^{17}\ \mathrm{eV}}\right) \tag{5.2}$$

where θ is the shower zenith angle, and E is the shower energy.

The signal density $\rho(r)$ is expressed in units of vertical equivalent muons per square meter (VEM m^{-2}), obtained by dividing the total observed signal by the average value from a vertical through-going muon. Use of this density unit allows simple calibration of water Čerenkov detectors using background muons. The slope parameter η is a function of zenith angle θ and, to a minor extent, shower energy.

For the highest energy showers, Equation 5.1 is replaced at $r > 800$ m by the modified expression

$$\rho(r) = kr^{-\left(\eta+\frac{r}{4000}\right)}\left(\frac{r}{800}\right)^{1.03}. \tag{5.3}$$

Equations 5.1–5.3 were seen to do an excellent job of describing data over the the entire measurement range (in the last chapter, Figure 4.6).

Figure 5.11 compares sets of Monte Carlo events with the Haverah Park experimental parameterization. Two cases are shown here, one for proton and the other for iron primaries. Each set was incident vertically and had primary energy of 10^{19} eV. The lateral distribution shape given by Equations 5.1 and 5.2 has been used in fitting the normalization constant k in the region $400 < r < 800$ m. For $r > 800$ m the flattened extension given by Equation 5.3 is shown, but this data was not used in the fit. The qualitative agreement in the shape is good, particularly for the iron primary simulations. This is shown on the right side of the figure where the ratio of the simulation points to the Haverah Park function is given. (Note that there is a slight overall normalization offset in the ratio plots; see the discussion of the parameter r_k in the next part of this section.)

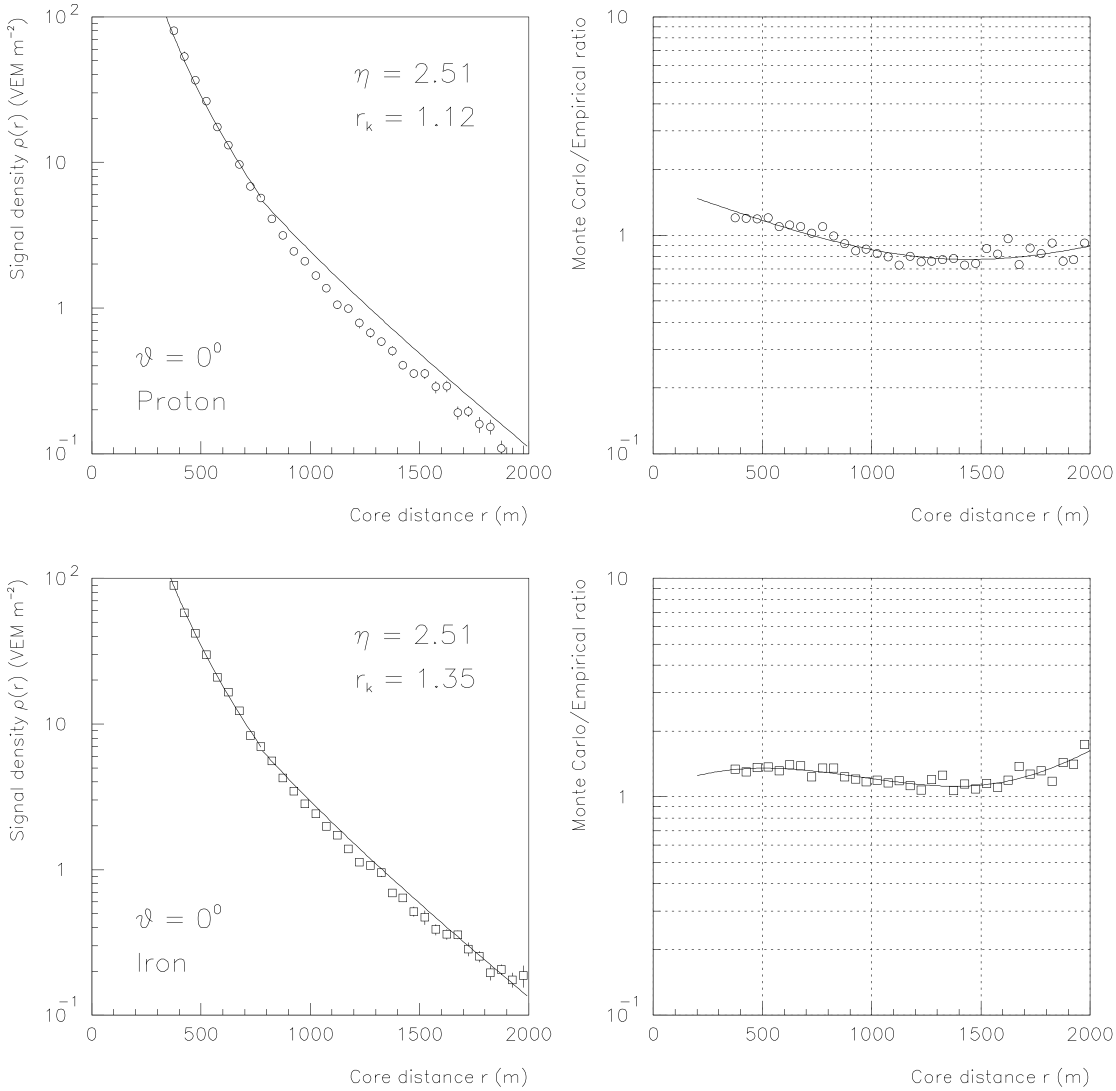

Figure 5.11: Left, comparison of simulated lateral distribution against measurements from the Haverah Park array. The points are Monte Carlo predictions for 10^{19} eV EAS, the lines experimental parameterizations given by Eqns. 5.3-5.2 in the text. The lateral distribution functions were computed using the indicated values for the slope parameter η and normalization correction r_k (see text and Table 6.1). On the right side, the ratio of the simulated points to the function; here, the lines are only to guide the eye.

As in the previous figure, Figure 5.12 shows comparisons for iron and proton primaries, except here the results are given at various zenith angles. The shower-plus-detector Monte Carlo reproduces the change in slope parameter η with increasing zenith angle θ. When showers are observed at increasing angles from the vertical, and hence at greater atmospheric depth, the lateral distribution "ages" or flattens, i.e. the slope parameter η decreases. Note that at large zenith angles protons and iron showers of a given energy produce very similar lateral distribution shapes. This is expected since the electromagnetic cascade has been almost entirely absorbed. The shape of the muon distributions in the two kinds of shower increasingly resemble one another as showers age beyond their maxima. The ability of the simulations to reproduce so well the change of η with zenith angle is a very encouraging result.

It is also seen in Figure 5.12 that the Haverah Park lateral distribution function appears to show slightly better agreement with the simulated iron showers than with the proton ones. This may be interpreted as a feature of the shower Monte Carlo rather than a real physical result. As discussed earlier, the number of muons at the ground is affected by the choice of hadronic model. This effect is not enormous but variations in the modeling may be sufficient to produce a better fit for proton primaries; further investigation is required. It is to be stressed that the effects of model assumptions do not seriously alter our calculations concerning the design of the array, but should be examined when performing detailed analyses of cosmic ray composition.

Lateral distribution normalization

The normalization constant k in Equations 5.1 and 5.3 is a function of shower energy and zenith angle. To account for the attenuation of a shower through the atmosphere, define a new density parameter $\rho_\lambda(600)$ by the relation $\rho(600) = \rho_\lambda(600)e^{-(\sec\theta-1)1018/\lambda}$, appropriate for the 1018 g/cm^2 atmospheric depth of the Haverah Park location. The measured value of the attenuation length λ at r =600 m was 760 ± 40 g/cm^2.

In the Haverah Park experiment shower energy is expressed in terms of $\rho_\lambda(600)$. When fitting experimental shower data with a free slope parameter, such as η, and using relatively few measurement points, errors in core location and slope parameter are interdependent. However, it turns out that the associated error in function normalization is on average minimal at a distance from shower core close to the array spacing distance (which for the Haverah Park system was typically 600 m). Simulations also suggest that shower-to-shower fluctuations produce smaller variations in density with increasing core distance, and that density dependence on primary particle mass is minimal near 600 m.

The relationship between primary energy, and lateral distribution normalization can only be determined from detailed calculations of shower development. Early Monte Carlo simulations by A. M. Hillas lead to the adoption of the relation $E = 7.04\times10^{17}\rho_\lambda(600)^{1.018}$ eV (where ρ_λ is in units of m^{-2}), for the Haverah Park array. This relationship is sensitive to experimental details, and so will differ somewhat from that obtained, for example, from Akeno data.

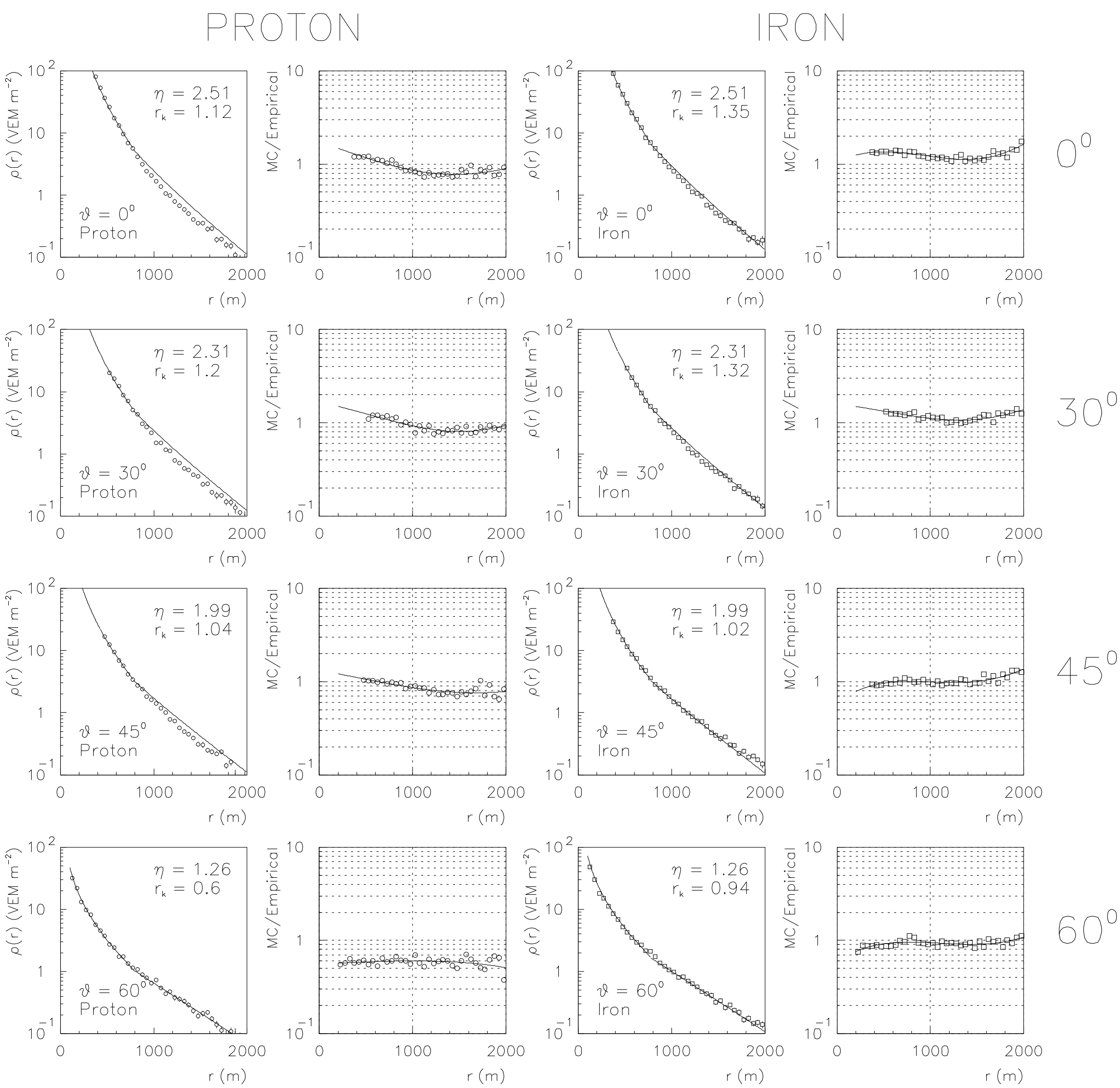

Figure 5.12: Comparison of simulation lateral distributions against measurements from the Haverah Park array, as in the previous figure. Here, simulated iron and proton showers at various zenith angles are shown.

Zenith angle (deg)	r_k (p)	r_k (Fe)
0	1.12	1.35
30	1.20	1.32
45	1.04	1.02
60	0.60	0.94

Table 5.1: Ratio of the fitted k parameter in normalization of the lateral distribution to the predicted value. Separate fits of the Monte Carlo data in the region $400 < r < 800$ m were done for protons and iron primaries at various zenith angles.

The above two relationships allow calculation of the expected value of the normalization constant k in Equation 5.1 for given shower energy and zenith angle. The quantity r_k (shown above in Figures 5.11 and 5.12) is the ratio of the k value determined by fitting the expected lateral distribution shape to the Monte Carlo data in the region $400 < r < 800$ m relative to the predicted value of k. For vertical showers the absolute normalization is the same to $\leq 35\%$. This is no more than saying that the new Monte Carlo reproduces the result of the old. However, the atmospheric attenuation with increasing zenith angle is also relatively well reproduced; Table 5.1 shows the values of r_k for proton and iron initiated showers at four different zenith angles. Note that the attenuation coefficient used is only known to be correct for $\theta < 45°$.

Shower front rise time

The timing structure of a shower front is greatly affected by muons. In a water Čerenkov detector at large distances from the shower core a significant fraction of the total signal is due to muons. (The simulations predict $\approx 20\%$ at 0.5 km rising approximately linearly to 50% at 1.5 km, increasing somewhat with primary particle mass and zenith angle.) Muons scatter less than the electromagnetic particles and so tend to arrive earlier. So muons will also tend to dominate the signal if one considers only the earliest arriving particles. From simple geometry alone, if a shower is approximated as a line source of muons, then in a shower developing high in the atmosphere the path length differences between muons from the top and bottom of the hadronic cascade will be smaller than for showers lower in the atmosphere, leading to a smaller dispersion in their arrival times. Note also that showers initiated by primaries of higher mass are expected not only to be on average higher in the atmosphere, but also to have a larger ratio of muons to electromagnetic particles, and hence a greater muon signal fraction (recall Figures 5.6 and 5.7). All of the above effects produce a correlation between signal rise time and primary particle mass at a given core distance.

At Haverah Park the water Čerenkov detector output pulses were integrated, displayed on oscilloscope screens, and recorded photographically. It was straightforward to measure not only the total time integrated amplitude, but also the arrival time dispersion of the air shower signal. The parameter chosen was called t_{10-50}, defined as the time taken for the trace to rise from the 10% to the 50% levels relative to the eventual total.

Figure 5.13 shows a comparison of the Monte Carlo predictions of t_{10-50} against actual data from the Haverah Park archives using the cuts indicated. The qualitative agreement is good, particularly for the simulated iron showers. However, the same caution which applies to interpretation of the lateral distribution shape agreement also applies here. The disagreement at $r < 600$ m for the showers at $\theta = 60°$ is partly due to bandwidth limitation effects in the Haverah Park electronics.

As a final comment, the differences in rise time between iron and proton showers is greatly reduced if one instead considers the majority (say, 90%) of the particles instead of only the first 50%. This effect is described later (Chapter 8) in relation to constructing an event trigger which is unbiased with respect to composition.

5.2.5 Reconstruction of simulated events

Analysis of the simulated events is done to estimate the ability of the Auger Observatory's detectors to achieve the physics goals. Given below are results of work on estimating the trigger efficiency, the accuracy of energy and direction reconstruction, and the separation of proton and iron induced showers.

Triggering

Schemes for triggering an array of water Čerenkov detectors have been implemented in the simulation. As mentioned before, the signals of photomultipliers are carefully simulated, including the digitizing electronics. One specific feature incorporated in the triggering simulation is that the muon signals are "clipped", i.e., the magnitude of the largest pulses are not permitted to exceed modest levels in the formation of alerts. This will allow the detectors to register the time dispersed signals expected from large showers far from their cores without contamination from the high rate of fast, large pulses from random single cosmic ray muons. The motivation is to have only those ground stations with activity beyond noise levels contribute to the formation of shower triggers. This scheme has been used successfully by many experiments (such as CASA-MIA). Hardware for this purpose is incorporated in the electronics and is described in Chapter 9. This detector alert condition is done in hardware within individual stations and does not involve communication with neighbors.

It is useful to impose a *minimum* time requirement on the formation of an alert in a ground station in order to combat detector noise. The signal must not only be large enough, it must also *not* be very short in duration. The time width of a signal grows with the primary energy, so very low energy showers (the source of much of the detector noise) tend to have rather short signal durations. The rate of random alerts in individual stations can be several kHz due in part to lower energy ($\geq 10^{14}$ eV) air shower particles. MOCCA simulation of lower energy showers indicates that the time width of the shower front near the core of these showers is very much less than the μsec widths of useful (10^{19} eV) showers at core distances of order a kilometer. If one requires that the particles in a station arrive over a time *longer* than 200-500 nsec, alerts arising from air showers with energy $< 10^{16}$ eV are effectively

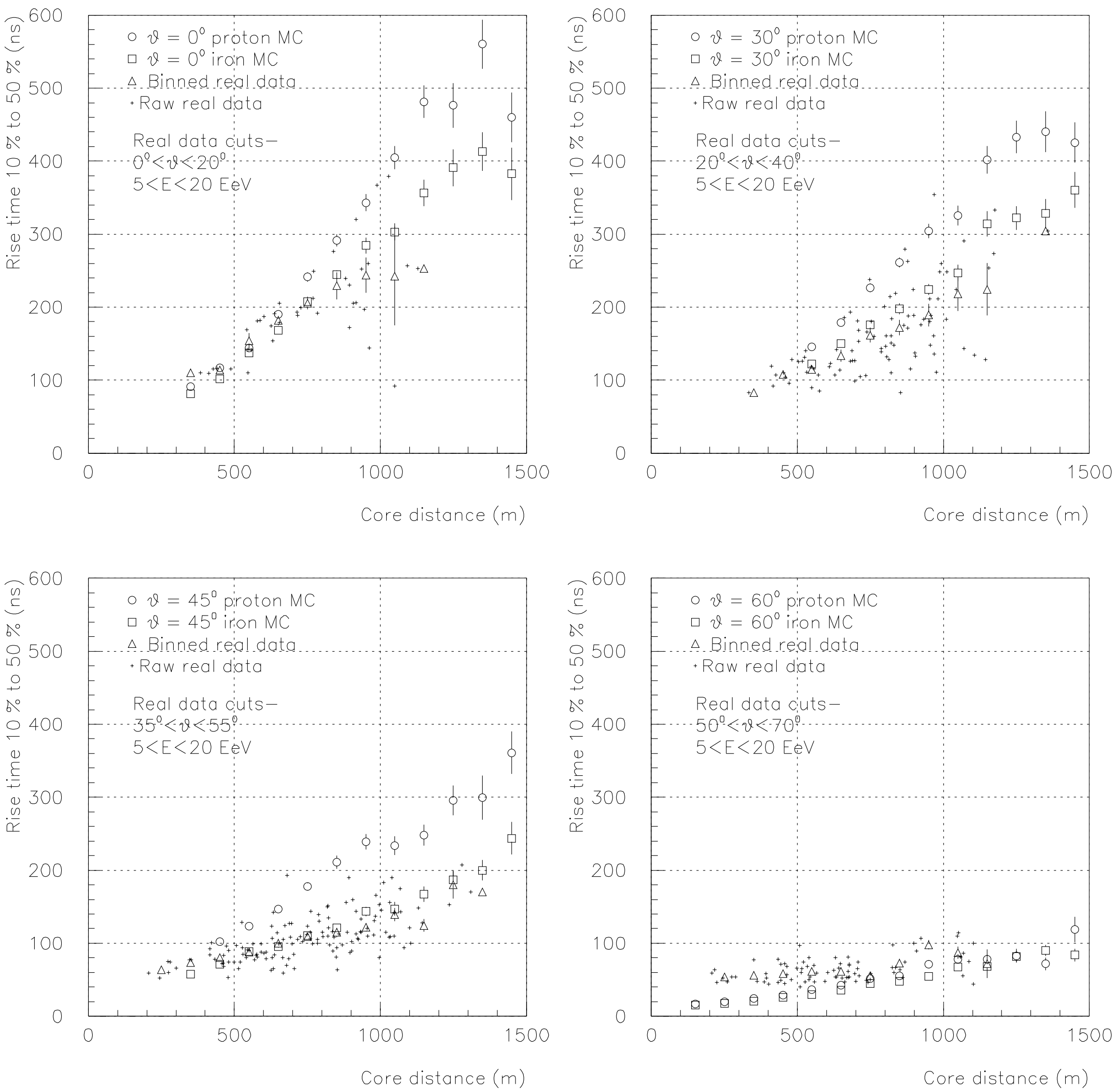

Figure 5.13: Comparison of simulated rise time against real data from the Haverah Park experiment. Comparisons are shown at zenith angles of 0, 30, 45 and 60 degrees. The "raw, real" observations have been extracted from the Haverah Park archives applying the data cuts indicated.

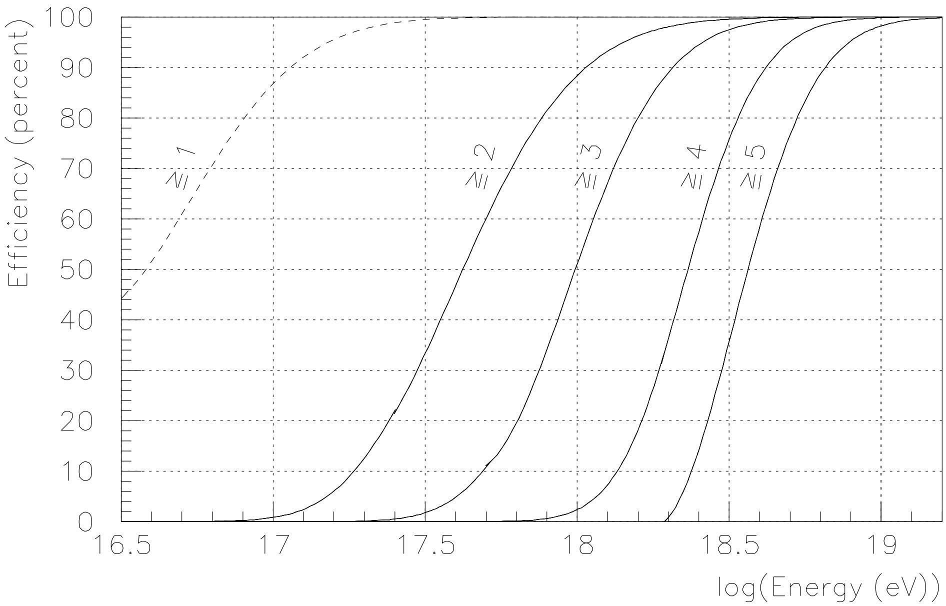

Figure 5.14: Trigger efficiency versus primary energy for vertical proton showers from MOCCA. Various alerted station multiplicity requirements are shown. Lower levels (and consequently lower energy) will be possible using additional constraints, such as separate triggers from the optical detector.

eliminated and so random noise is substantially reduced.

The shower trigger is formed by requiring some minimum number of stations to report coincident alerts within a minimum time. Figure 5.14 shows the efficiency at which vertical proton showers of various energies will trigger the array. Requiring 5 or more alerted stations within 20 μsec gives good efficiency at 10^{19} eV. Also shown are the efficiency curves at lower multiplicity requirements. While such low levels tend of course to eventually become noise-dominated, it will be possible to retain events with the additional constraint of requiring a separate trigger from the fluorescence detector. The reduced energy threshold of the ground array at the lower multiplicity levels (between 10^{17} eV and 10^{18} eV) is well matched to optical detectors such as those described in subsequent chapters.

Most showers recorded by the array will not be vertical. Figure 5.15a shows the 5-fold trigger efficiency and mean alert multiplicity for more typical events (30° from the zenith).

Direction Reconstruction

The determination of the arrival direction of a primary cosmic ray is done by reconstructing the resultant air shower geometry. Particles arrive at the ground in a shower front with a conical shape and a thickness of a few μsec (recall Figure 5.3 and Figure 5.4). If more than three ground stations report hits then the shower front geometry can be fit from the recorded arrival times.

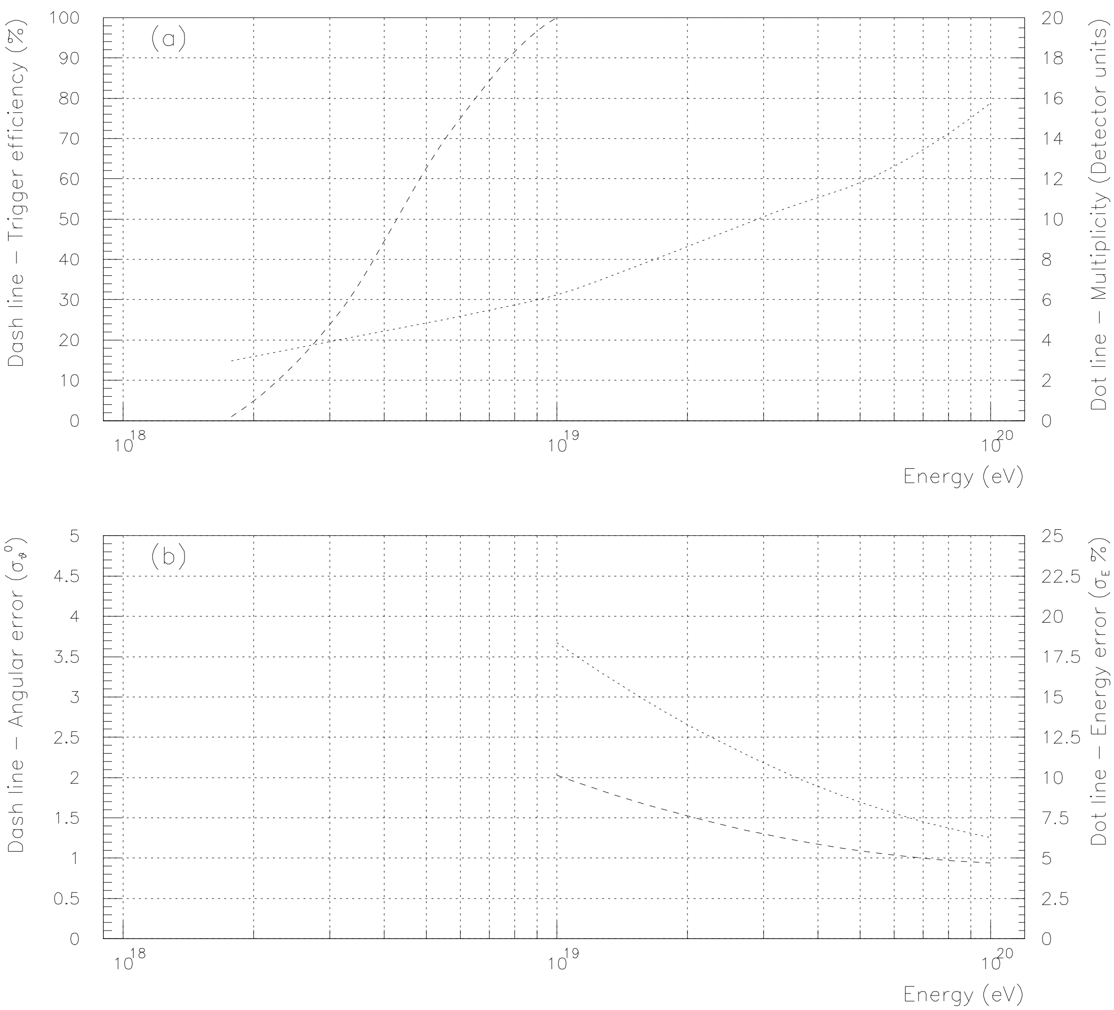

Figure 5.15: Summary of Auger Observatory water Čerenkov surface array performance as determined by reconstruction of simulated events. The upper plot shows the detector unit multiplicity and array trigger efficiency if 5 fold events are demanded, for proton showers at 30° (compare to last figure which used vertical showers). In the lower plot, expected reconstruction accuracy of direction and energy for vertical proton showers. The energy error plotted is only the random component due to detector physics and statistics. The estimated shower-to-shower fluctuations contribute 10% to the energy resolution, which should be added in quadrature with the values shown. The assumption of primary particle type results in a systematic shift of at most 25%. This systematic shift can be substantially corrected using rise time measurements, muon counting, and X_{max} measurements. The corrections can be calibrated and confirmed using hybrid data.

The detector simulation described above is used to provide realistic timing information (including the intrinsic dispersion in the shower front) for alerted ground stations. The precision of the signal digitizing electronics and GPS systems is taken as 5 nsec. The times are those of the first particle to strike each detector. The fit itself is a least-squares minimization of the difference between the recorded times and those expected from the arrival of a plane whose orientation is varied. A conical geometry should properly be used to fit the times, but if the core of the shower is not near the array boundary a plane fit works nearly as well and is insensitive to the location of the core.

The accuracy of the fit is determined by comparing a vector normal to the best-fit plane to the true direction of the shower. Under the assumption that the probability of observing some angle between these vectors is distributed as a symmetric two dimensional Gaussian function, Figure 5.15b shows the resulting σ obtained from our simulations. Alternatively, define the parameter σ_{63} to be the space angle with respect to the true direction within which 63% of events have been reconstructed. This parameter is commonly quoted as the "angular resolution" of an experiment since it is closer to the optimum signal-to-noise acceptance cone when searching for a point source in the presence of a uniform background. Note that σ_{63} can be easily computed without having to fit an assumed error distribution function. If the error distribution happens to be Gaussian, then $\sigma_{63} = \sqrt{2}\sigma$. We find that $\sigma_{63} = 3.0°$ for vertical 10^{19} eV proton showers. The accuracy improves to about 1.3° at 10^{20} eV.

The geometry of water Čerenkov detectors is such that longer track lengths and consequently larger individual muon signals occur for showers away from the vertical. This causes the angular reconstruction accuracy to actually improve at large zenith angles. At 60°, for example, $\sigma_{63} = 1.3°$ at 10^{19} eV and 0.5° for 5×10^{19} eV.

Reconstructions of iron showers at similar energies and zenith angles show slightly better angular resolution than proton showers. This presumably arises because the fitting procedure uses the times of the first arriving particles at each detector. Muons tend to be the earliest arriving particles in any air shower. Iron showers have more muons than proton showers of the same total energy, and so appear "bigger" when measured this way, with a corresponding improvement in reconstruction accuracy.

Energy Reconstruction

Algorithms for reconstructing the energy of the air shower have been developed using fits to the observed signal density at a specific core distance (600 m). Event reconstruction is done using standard least square fit methods. The Haverah Park experimental parameterization of the water Čerenkov lateral distribution given by Equations 5.1–5.3 is used. The Haverah Park attenuation coefficient is also used to predict normalization shift at increasing zenith angle. Using a maximum likelihood technique, the energy of the shower is computed using a fitted size-energy relation obtained previously from an independent set of analyzed MOCCA showers.

Firstly, assume that the nature of the primary composition is known so that proton showers are fitted according to relations appropriate for protons. The error distribution of the reconstructed energy of the detectors is found to have a log-normal distribution (i.e., the distribution of log(E) has a Gaussian shape), with a standard deviation shown in Figure 5.15b. Note that the standard deviation of the distribution of log(E) is equivalent to the relative error in the energy, σ_E/E.

The reconstruction accuracy shown under these assumptions reflects only the random component from the sampling statistics of the detectors. This approach is relevant for showers with a single nuclear component or where the nature of the primary can be determined by other means, either from optical detector measurements or muon measurements. To avoid this requirement, the fits are also performed using an average of the lateral distribution functions of protons and iron. The accuracy of this method will depend on the true composition of the primary cosmic rays.

By means of a simple numerical exercise, estimates have been made as to whether the energy reconstruction will be sufficiently accurate to achieve the goal of identifying features in the cosmic ray energy spectrum. This is neither a detector nor a shower simulation, but rather an exercise to see the effects of "smearing" energies drawn from an assumed parent distribution. In particular, it investigates the degree to which energy resolution will distort the features of a spectrum which is, overall, steeply falling.

Shower energies are generated according to an input spectrum having an $E^{-2.5}$ power law character and a GZK cutoff [132]. The effects of triggering are estimated by accepting a fraction of the generated events according to the probability that five or more surface stations are alerted (from Figure 5.14). Each accepted energy is then altered according to a Gaussian distribution of $\log_{10}$(E) to approximate the effects of reconstruction. The variance of this distribution includes both random errors as described above and another term corresponding to uncertainty in the primary composition which is assumed to be equal parts iron and protons. The two effects are added in quadrature. The net smearing of $\log_{10}$(E) is equivalent to a relative error ($\delta E/E$) of about 25% at 10^{19} eV, improving to about 20% at 10^{20} eV. Note that the procedure is conservative and would overestimate the energy smearing of a sample of events which are dominated by a single nuclear type.

The "reconstructed" energy spectrum is compared with the input. Figure 5.16 indicates how well an assumed cosmic ray energy spectrum can be measured in this way. In this plot, the total number of events corresponds to about 1.7 years of operating the full Auger Observatory. It is clear that this level of resolution will permit the observation of the GZK cutoff. Rough inspection of the reconstructed spectrum suggests that changes in the power law slope of as small as 0.2 or features (bumps) greater than about 30% of the baseline power law can be discerned in this sample.

Also note that a significant number of events below 5×10^{18} eV will be obtained, despite low trigger efficiency, because of the steep spectrum of cosmic rays.

Composition Sensitivity

The simulated signal timing-amplitude profiles have been analyzed to determine the muonic signal fraction, and hence to separate showers on the basis of primary particle type. Large

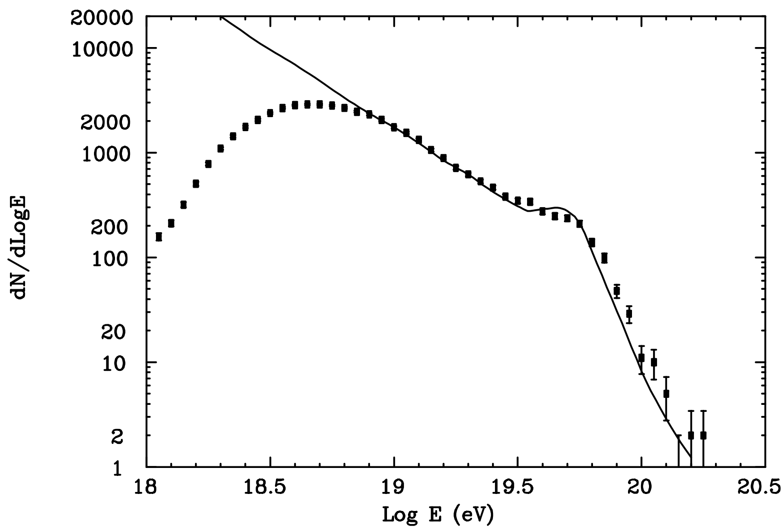

Figure 5.16: Reconstructed energy spectrum of cosmic rays, assuming an input spectrum shown with the solid line, an $E^{-2.5}$ power law and GZK cutoff. The points are from simulation corresponding to about 1.7 years operation of the Auger Observatory.

narrow pulses in the simulated detector signals are identified using a pulse height threshold criterion in the analysis (recall Figure 5.10). The fraction of the integrated signal contained therein is taken to represent the ratio of muons to electrons. The discussion in the last chapter illustrated an example of this technique. It is likely that this can be improved, either through optimizing the selection technique or perhaps by increasing the tank depth from 1.2 m to about 2 m.

Estimates of the nuclear composition as described in the last chapter could be made by constructing the μ:em parameter for events and comparing them to the curves shown. Also, considering that the composition may not be dominated by a single nuclear type, the *width* of the μ:em distribution for a sample of data can also be calculated and compared to the prediction of the simulation. This technique gives information on whether the composition is in fact mixed or pure and whether it is heavy or light. Such an approach has been employed previously by the Fly's Eye group.

Note that the muon/electron ratio measurements for the purpose of studying composition are relatively insensitive to changes in the physics models of the simulation at extreme energy. As mentioned earlier (Figure 5.1), most ground-level particles originate from the lower energy interactions in the shower where the modeling has been well calibrated by accelerator experiments.

Again, caution must be applied when evaluating these reconstruction results. Although statistical and detector-imposed fluctuations are included in the simulation procedure, the shower-to-shower fluctuations caused by variations in depth of first interaction, etc., have been averaged out by the process used to overcome the "thin sampling" limitations of MOCCA. Some results may also be optimistic due to the lack of simulated events at the "edges" of the array. Work is on-going on more realistic simulation.

5.3 Hybrid Detector Simulation

The simulation methods employed to evaluate the performance of a Hybrid detector are described here. The term "Hybrid" refers to the combination of a ground array and an atmospheric fluorescence detector. Advantage has been taken of the experience and existing detector simulation code from two groups - the ground array simulation code of the AGASA experiment, and the HiRes detector Monte Carlo. Both simulations have been developed over long periods, and have been refined using results from observations. Elements from both sources have been combined to first study the geometrical reconstruction accuracy of a Hybrid detector, using the ground array shower arrival time as a constraint in the fluorescence detector determination of the shower direction and core. The various elements of the simulation are described, from the shower generation through to detector modelling.

A three-eye fluorescence system is investigated. For the most part, showers are viewed by a single fluorescence detector in conjunction with the ground array, although at the highest energies some showers will be viewed by two or three eyes. Each eye images the sky up to an elevation angle of approximately 30° with 1.5° diameter pixels.

It will be shown that a shower viewed by a combination of a single fluorescence site and the ground array will be reconstructed with an accuracy equivalent to that given by a stereo fluorescence system, where showers are viewed by two fluorescence detectors without a ground array. (The latter technique, called "stereo" reconstruction, is the method employed by the HiRes detector). Based on the solid footing of good geometrical reconstruction, the energy and depth of maximum resolution of the Hybrid detector will be discussed.

Generic fluorescence and ground array detectors have been used in this study. For example, the fluorescence detector uses mirrors and phototubes in the classic Fly's Eye approach, and the ground detector consists of an array of scintillators with the characteristics of the AGASA detectors, though with each detector having a larger area. Variants on these designs (i.e. for example replacing the scintillator detectors with water detectors of the same area and on the same grid spacing) will have only a small effect on the geometrical reconstruction accuracy, and hence a small effect on the fluorescence detector determination of energy and depth of maximum.

5.3.1 Methods

In our simulations of the Hybrid aperture, geometric reconstruction, and energy and X_{max} resolution, parametrizations of the longitudinal and lateral structure of the showers were used. Fluctuations were introduced where appropriate. Each parametrization is discussed in turn.

Longitudinal Profile

Each simulation was performed at fixed energy. For each energy, the *mean* depth of shower maximum was determined from simulations [133]. Results appropriate to a proton primary beam have been used, with a X_{max} of 780 g cm^{-2} at 10^{19}eV and an elongation rate of 55 g cm^{-2}. Such a composition is consistent with the Fly's Eye data above 10^{19}eV.

Variations in the depth of maximum were simulated simply by introducing fluctuations in the depth of first interaction X_0. A mean interaction length of 70 g cm^{-2} was assumed at all energies. This is clearly not accurate, though it is sufficient for our investigation of detector aperture, geometrical reconstruction and energy and depth of maximum resolution.

The primary energy determines the shower size at maximum, N_{max} [134]. Given N_{max}, X_{max} and X_0, the complete longitudinal profile was described by the Gaisser-Hillas function [135].

Charged Particle Lateral Distribution

The AGASA lateral distribution function has been used to determine the particle counts in the ground detectors. The function is given in [15] and has a dependence on shower zenith angle. The shape of the function has no energy dependence, since none has been detected in the AGASA data.

The shower size at ground level (the normalization of the lateral distribution) is determined from the longitudinal profile discussed above, and the shower zenith angle. In this way the development fluctuations introduced in the fluorescence simulation are passed onto the ground array simulation.

Shower Front Timing Structure

To handle the shower front curvature and thickness, data tables of the delay of shower particles behind an imaginary plane shower front have been constructed using an ensemble of MOCCA-generated vertical proton showers at 10^{19}eV. These include the response of standard AGASA-type scintillators to low energy gammas and electrons. These tables are embedded into a subroutine which, given the core distance, assigns a particle an arrival time with respect to a plane shower front. In other words, both the curvature and the thickness of a shower front are simulated in a reasonable way.

5.3.2 Simulation of Fluorescence Detector Response

Three eyes are placed on the vertices of an equilateral triangle, 32.7 km on a side. A total of 1596 ground array detectors are arranged over an area defined by a "superman" outline (Figure 5.17). Each eye views the sky up to an elevation angle of 30° over the full azimuth range. There are 45 mirror units per eye, 23 in the lower ring and 22 in the second ring.

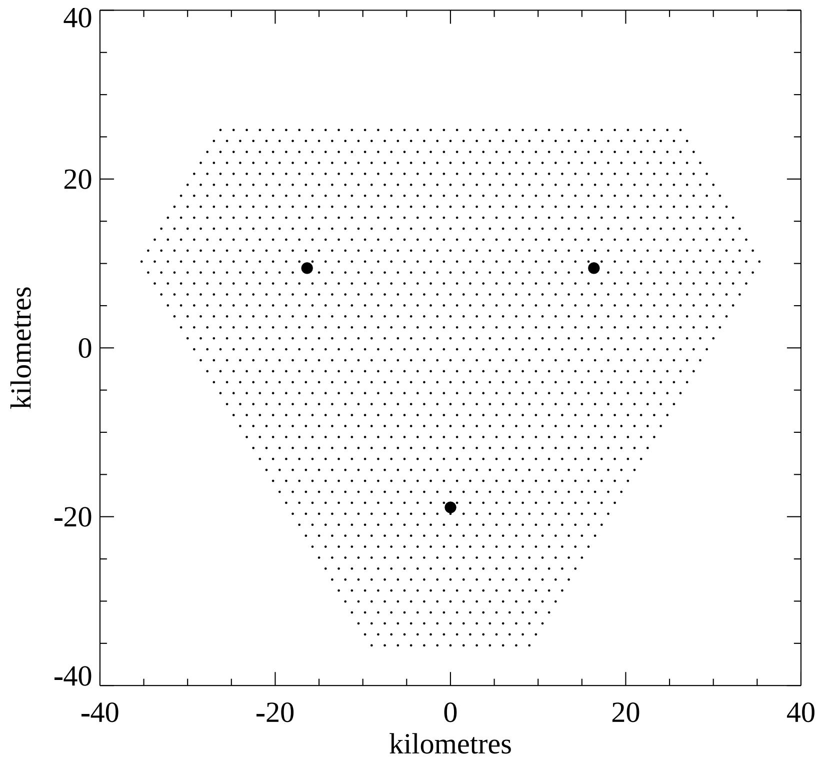

Figure 5.17: The positions of the three fluorescence detectors and the 1596 ground array detectors in the Superman arrangement.

Each mirror has an unobscured area of 1.54 m^2 (actual diameter 1.5 m) and each images the sky onto a cluster of 121 hexagonal photomultipliers (pmts). A single pmt views a solid angle equal to that of a circular pixel with diameter 1.5°. There are 5445 pmts in each of the three eyes.

The fluorescence simulation code is based on the HiRes Monte Carlo program. The phototube triggering thresholds are set by comparing the expected night sky noise level with that seen by HiRes. Given that the sky background light scales with the product of mirror area A and the solid angle viewed by a phototube Ω, the noise scales as $\sqrt{A\Omega}$ for AC-coupled electronics. Thus comparing the sky noise in the 1.5° pixel system with HiRes,

$$\frac{N_{1.5^\circ}}{N_{\mathrm{HiRes}}} = \frac{\sqrt{A_{1.5^\circ}\Omega_{1.5^\circ}}}{\sqrt{A_{\mathrm{HiRes}}\Omega_{\mathrm{HiRes}}}} = \frac{\sqrt{1.54 \times (1.5^\circ)^2}}{\sqrt{3.75 \times (1^\circ)^2}} = 0.96$$

Thus, in the simulation individual pmt triggering thresholds are set at 96% of the HiRes levels.

The calculations are performed for an atmospheric depth of 860 g cm^{-2}. An outline of the simulation follows. Details of some of the methods used here can be found in [8, 136].

1. For a chosen energy determine the shower depth of maximum. Randomly choose shower arrival direction (zenith angle less than 60°) and core location. The core location must lie within the physical area of the ground array.

2. Calculate light emitted from the shower along its track. Both fluorescence and Cerenkov light is calculated. The pressure and temperature dependence of the fluorescence yields are taken into account.

3. Calculate the light yield arriving at the detector site. Rayleigh and Mie scattering processes are simulated, with full account taken of the spectral characteristics of the light. The isotropically emitted fluorescence light, as well as direct and scattered Cerenkov light, is propagated. Night sky background noise is added to the signal.

4. Mirror area and reflectivity are used to determine the light falling on each phototube cluster. Optical filter transmission and phototube quantum efficiency factors are folded with the light spectrum to give the photoelectron yield in each tube, due to signal and noise.

5. For each tube viewing the shower, the photoelectron yield, the pulse width and an estimate of the time at the midpoint of the pulse are recorded. These parameters are calculated assuming that the mirror produces a Gaussian-profile light spot in the focal plane with a fixed standard deviation of 0.25°. The mid-pulse time is calculated, then fluctuated, using experience with the FADC system currently being constructed for HiRes. The uncertainty of the mid-pulse time is a function of the pulse width and the number of photoelectrons.

6. A phototube is said to trigger if its instantaneous photoelectron current (taking into account the time constant of the circuitry) is greater than the 4σ night sky noise level. A mirror will trigger if it contains a sufficient number of firing tubes. Here we demand that the track length of firing tubes within a mirror exceeds 9°.

7. A trigger in at least one mirror defines an accepted event. The data from all firing tubes in the detector (even in mirrors not satisfying the track-length requirement) are recorded.

5.3.3 Simulation of Ground Array Response

The main steps of this procedure are taken from the AGASA detector Monte Carlo [15]. The array consists of 10 m^2 detectors made of 5cm plastic scintillator arranged on a triangular grid of spacing 1.5 km. The procedure is as follows,

1. Energy, shower direction and core location come from the fluorescence section of the simulation.

2. Determine the shape of the lateral distribution, a function of zenith angle.

3. Determine the ground level shower size from the profile used in the fluorescence calculation. In this way, fluctuations in the depth of maximum are translated into shower size fluctuations at the array. The shower size provides the normalization for the lateral distribution, which is used to calculate the particle count n_i in each detector.

4. Determine the number of particles registered by each detector by sampling from the Poisson distribution with mean n_i.

5. Each particle is assigned an arrival time relative to a plane shower front, using the data tables discussed earlier. The time of arrival of the first particle is recorded, as well as the mean arrival time and time dispersion of all the particles. It is assumed that each detector is equipped with FADC-like electronics with a sample rate of 40 MHz. (A systematic study of the effect of finite array timing resolution on hybrid reconstruction has been performed. It appears that there is little effect on reconstruction until sample rates fall below 10 MHz [137]).

6. Detector resolution is folded into the particle density. This is based on results from Akeno detectors in the 1 km^2 array.

7. For an event to trigger the array, it is required that at least three stations register a particle count greater than 3. (For simulations at 10^{18}eV and 3×10^{18}eV the station requirement is relaxed to two, provided that a coincident fluorescence detector trigger is present). No pulse width discrimination is applied. Once a trigger is established, record data from stations with particle counts of at least one particle. This approximates a possible real trigger scheme.

5.3.4 Hybrid Geometric Reconstruction Method

A reconstruction method using the fluorescence detector alone is presented below, followed by a method of adding ground array information to constrain the fluorescence fit.

Fluorescence Detector Geometric Reconstruction

The standard single-eye fitting procedure for the shower core location and direction starts with the determination of the plane containing the shower axis and the center of the eye. This shower-detector plane (SDP) fit uses tube pointing directions, together with signal integrals. Tube timing information is not used at this stage, except to discard noise tubes.

The SDP fitting procedure as used with the HiRes detector is described in detail in [142]. Briefly, trial planes are compared with the pointing directions of fired phototubes, with the fit weighted by the signal amplitudes. Pulse width information, which would be available with Flash ADC electronics, has not been exploited. The pulse width would help determine the crossing point of the shower image across each tube and constrain the plane fit even further.

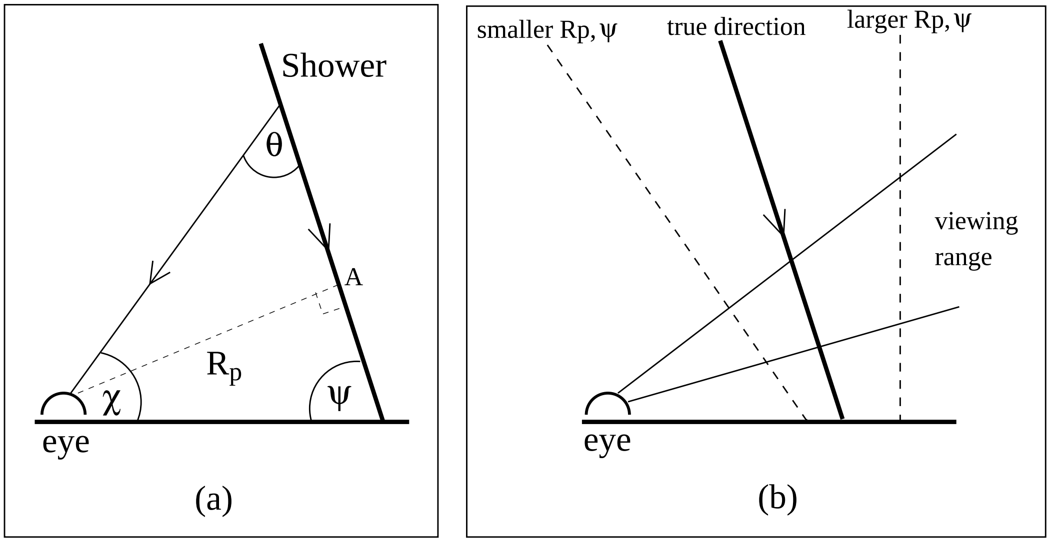

Figure 5.18: (a) Geometric reconstruction within the shower-detector plane. A phototube views the shower at an angle θ with respect to the axis. (b) Ambiguity in the position of the shower within the SDP for short tracks (highly exaggerated). Each of the three shower tracks shown would pass through the detector's field of view with similar (and approximately uniform) angular velocity.

Once the SDP is determined, the firing times of the tubes are used to determine the orientation of the shower axis within that plane. The times used here are estimates of the time at which the tube integral reaches 50% of its full value. This is our estimate of the tube-centre crossing time. Figure 5.18(a) shows the geometry within the SDP. For a given geometry, the arrival time of light at a tube viewing the axis at an angle θ_i is

$$t(\theta_i) = \frac{R_p}{c} tan(\frac{\theta_i}{2}) + t_0$$

where t_0 is the time at which the shower reaches point A on the diagram, and $\theta_i = \pi - \psi - \chi_i$. A fit is done for R_p and the ground angle ψ. Together with the SDP, these parameters fully define the event geometry.

There is a problem with these timing fits, especially for short (i.e. distant) shower tracks. This has long been recognised, and is one reason the stereo Fly's Eye technique was pursued as an alternative to mono observations. With short tracks it is often the case that the range of θ_i sampled is not large enough to detect significant curvature in the tangent function in the above equation. In other words, the shower appears to pass through the field of view with *constant angular velocity*. Unfortunately, this leads to ambiguity in the fit, with a family of possible (R_p, ψ) values (Figure 5.18(b)).

Hybrid Geometric Reconstruction

This ambiguity can be resolved by using other information, for example a SDP from another fluorescence detector, or information from a ground array. The most promising ground array parameter is the arrival time of the shower at the ground [143]. It is obvious from Figure 5.18(b) that if all eye and ground array times are measured with a common clock, then the ground array times will constrain the timing fit within the SDP.

The full Hybrid geometrical reconstruction proceeds in the following way:

1. The SDP is determined in the standard way, using fluorescence information only. Typically, the plane orientation is known to better than 0.25°, which corresponds to a distance of at most 60m on the ground at a distance of 15km. Thus ground array information is of limited use at this stage of the fit.

2. From this point on it is assumed that the shower core is contained on the line forming the intersection of the SDP and the ground. The timing fit is performed, minimizing a χ^2 which includes the standard fluorescence timing term and an array timing term. The fluorescence timing term is

$$\chi_1^2 = \frac{N_t}{\sum pe_i} \sum \frac{(t_i - t_{expected})^2}{\sigma_{ti}^2} pe_i,$$

   where t_i is the estimate of the pulse mid-point time, and σ_{ti} is the mid-point time uncertainty for each tube. The elements of the sum are weighted by pe_i, the signal in each tube. The sum is multiplied by N_t, the number of firing tubes, to give the appropriate weight to this term of the χ^2 when the array component is added.

3. The array component of the χ^2 may take one of three forms.

   (a) **Method 1:** The first method uses a single array detector to define the shower arrival time. The detector with the largest particle count is chosen, and a model of the curvature of the shower front is used to calculate the expected time in this detector for each trial geometry. The shower front curvature parametrization is the same one used in the generation of the data, but because this detector is close to the core, the dependence on details of the curvature is not strong. (In any case, it is expected that measurements of curvature will be one of the first tasks of the array). The χ^2 term is then

$$\chi_2^2 = \frac{(t_i^* - t_{expected})^2}{\sigma_{ti}^{*2}}$$

   where

$$\sigma_{ti}^* = \frac{\sigma_{0i}^*}{\sqrt{n_i^*}}$$

   and t_i^* is the mean arrival time of particles at the detector with the largest particle count, σ_{0i}^* is the dispersion in the arrival time, and n_i^* is the number of particles detected.

   (b) **Method 2:** While the method above is conceptually simple, it does not use all of the available array data. In the second method the mean arrival time of all array detectors with particle counts greater than 10 is used. The expected times are again calculated using the shower curvature parametrization used in the data generation.

The term is

$$\chi_2^2 = \sum \frac{(t_i - t_{expected})^2}{\sigma_{ti}^2}$$

where

$$\sigma_{ti} = \frac{\sigma_{0i}}{\sqrt{n_i}}$$

where the sum is over all detectors with particle counts greater than 10 particles. t_i is the MEAN arrival time of the particles at each detector, σ_{0i} is the dispersion in the particle arrival time, and n_i is the number of particles detected.

(c) **Method 3:** What if the form of the shower front curvature is not known? The following method was also found to work well. Again, times from all array detectors with particle counts greater than 10 are used. But here the time of the FIRST particle in each detector is used, and the expected time is calculated assuming a PLANE shower front. Surprisingly perhaps, this method works very well. It is true that the first particle will arrive closer to a plane front than the majority of the particles, which will be delayed. However, the success of this method probably relies on there being time measurements on all sides of the core. The method may produce a systematic error in direction for showers landing near the edge of the array.

The form of the χ^2 term is the same as in Method 2, but here t_i is the arrival time of the FIRST particle at each detector. Again σ_{0i} is the dispersion in the arrival time of all the particles, and n_i is the number of particles detected.

4. The final χ^2 minimization is performed on the linear sum of the fluorescence and ground array components, with the ground array component taking one of the three forms discussed above. That is,

$$\chi^2 = \chi_1^2 + \chi_2^2$$

Results from Methods 2 and 3 will be given below. For examples of the effectiveness of Method 1 see [144], a study of the "Cyclops" configuration of the Auger Observatory, in which a single large eye stands at the centre of a 3000 km^2 array.

5.3.5 Energy and X$_{max}$ Resolution

The ability of a fluorescence detector to make an accurate determination of a shower's longitudinal profile depends critically on the stage of analysis already discussed, the geometric reconstruction. Once a good geometry is determined, the conversion of measured light intensities into a longitudinal profile relies on an understanding of the light propagation properties of the atmosphere. The analysis assumes the same atmospheric parameters used in the generation of the simulated data. The model used is in excellent agreement with the "1976 US standard" atmosphere with a desert aerosol profile. It is assumed that the atmosphere at the observatory site (particularly the aerosol structure) will be monitored and characterised using lasers, in a way similar to that being used at the HiRes site.

The method used for profile reconstruction is that used in the Fly's Eye and HiRes experiments (see [8] for a description). Essentially, it is the reverse of the process described in the simulation section above. Photoelectron counts in a particular tube are converted to a shower size at the shower axis by a process which takes into account the physical parameters of the detector, atmospheric transmission and shower light production (fluorescence light and Cerenkov light, both direct and scattered). Finally, the Gaisser-Hillas function is fitted to the measured profile to extract the shower size at maximum, N_{max}, the depth of maximum, X_{max} and the depth of first interaction X_0. The energy is then determined by integrating the profile, and taking account of the small fraction of energy not carried by the electromagnetic portion of the shower.

5.3.6 Results

Figure 5.19(a) shows the Hybrid efficiency as a function of energy. Showers with random zenith angles up to 60° and cores within the bounds of the ground array were simulated, an aperture of 7069 km^2 sr. At least one eye and the ground array were required to trigger for the event to be accepted. The event was also required to successfully pass through the reconstruction procedures. Figure 5.19(b) shows one advantage of a three eye system - at the higher energies, many showers trigger two or three eyes.

For the following reconstruction studies, a single eye was chosen and showers were simulated over an area larger than its triggering aperture, so as to give a realistic collection of triggering events. While some showers will trigger more than one eye, this extra information has not been exploited in the current study.

Beginning with the geometry determined by the fluorescence detector alone, the error distribution for the *normal* to the shower-detector plane (SDP) is shown in Figure 5.20. All showers triggering the Hybrid detector at 10^{19}eV are used, and the differential and integral forms of the error distribution are shown. It can be seen that 50% of the plane normal errors are less than 0.22° and 90% are smaller than 0.80°.

Within the shower detector plane, the fluorescence detector uses tube firing times to determine the impact parameter R_p and the ground angle ψ (see Figure 5.18). The resolution of these measurements is strongly dependent on the length of the shower track viewed by the eye. Results are given for R_p in Figure 5.21, again for 10^{19}eV showers triggering the Hybrid array. Only fluorescence information is used in reconstruction here. Results for the ground angle ψ are included in Table 5.2.

Array information is applied to the fits using two of the three methods described earlier. (For examples of the efficacy of Method 1, see results from the "Cyclops Eye" simulations in

Meth.	Δdirec.(°)		ΔCore(m)		ΔR_p(m)		$\Delta\psi$(°)		$\Delta E/E$ (%)		$\Delta X_{\max}$(g cm^{-2})	
	50%	90%	50%	90%	50%	90%	50%	90%	50%	90%	50%	90%
10^{18}eV (median plane normal error 0.34°)												
2	0.54	1.71	35	183	20	90	0.32	1.17	8.6	43	32	135
3	0.49	1.85	35	188	18	101	0.27	1.29				
3×10^{18}eV (median plane normal error 0.31°)												
2	0.43	1.35	35	141	17	95	0.26	0.82	4.9	23	25	83
3	0.40	1.35	35	144	16	95	0.21	0.88				
10^{19}eV (median plane normal error 0.22°)												
0	2.5	19.8	350	5600	350	3300	2.5	19.7	9.4	55	31	158
2	0.35	1.03	29	98	15	74	0.21	0.71	4.2	18	17	60
3	0.31	1.08	29	101	13	68	0.17	0.55				
3×10^{19}eV (median plane normal error 0.21°)												
2	0.31	0.81	27	79	14	59	0.19	0.54	3.2	15	16	64
3	0.29	0.80	25	84	11	71	0.14	0.48				
10^{20}eV (median plane normal error 0.23°)												
2	0.36	0.87	29	90	14	71	0.22	0.69	2.5	17	15	70
3	0.29	0.70	28	80	12	60	0.16	0.46				
3×10^{20}eV (median plane normal error 0.22°)												
2	0.36	0.89	32	91	16	80	0.24	0.76	2.5	30	15	105
3	0.28	0.73	30	72	14	65	0.17	0.47				

Table 5.2: Reconstruction resolution values from various methods, for a single 1.5° pixel eye in a 3-eye system. The values of the error parameter bracketing 50% and 90% of the distribution are given. The energy and depth of maximum resolution was not calculated for Method 3. "Method 0" represents reconstruction using single-eye fluorescence information without ground array data.

[144]). Again for 10^{19}eV triggers, Figure 5.22 shows the impact parameter R_p distributions for (a) Method 2 and (b) Method 3. Note how the dependence on track length has dramatically lessened. Similar results are found for the ground angle ψ (Table 5.2). Both methods represent significant improvements over "fluorescence only" fits in the previous figure. A median R_p error of about 15 m is found using these methods.

The final core location and shower direction errors for events at 10^{19}eV are displayed in Figure 5.23 for Method 2 (Method 3 gives very similar results as seen in Table 5.2). The plots show a median core location error of 29 m and a median shower direction error of 0.35°.

Figure 5.24 and Figure 5.25 show results from the profile reconstruction for 10^{19}eV showers. As with all figures in this section, no quality cuts have been applied to the distributions. In Figure 5.24(a), the X_{max} error $(Xmax_{reconstructed} - Xmax_{true})$ is shown for showers analysed using the fluorescence information alone. Also shown are the results for the same showers analysed using Hybrid Method 2. Again, results from Method 3 are quite similar. Even with good geometrical reconstruction, it is clear that a long track length improves the reconstruction of the longitudinal profile. The poorer fits to X_{max} and energy are generally associated with short tracks.

Figure 5.25 shows the energy resolution $(E_{reconstructed} - E_{true})/E_{true}$ for 10^{19}eV showers analysed with (a) fluorescence information only and (b) Hybrid Method 2. Again the Hybrid method significantly improves the tails of the error distribution. Results from other energies are given in Table 5.2. The slight worsening of the energy and X_{max} resolution at the highest energy is a result of some near-vertical showers arriving at ground level before reaching their maximum size.

At an energy of 10^{18}eV the array described is not fully efficient. However, showers of this energy may trigger two or three array detectors. Figure 5.26 shows results for 10^{18}eV showers analysed using Method 2. The array triggering requirement has been relaxed at this energy to allow events to trigger with only two detectors at the 3-particle level (instead of three detectors). Method 2 uses array times from detectors with a particle count of at least 10. In some events this may mean that only one or two detector times are used in the fit. Despite this, good reconstruction appears possible for most showers. Results for Method 3 are given in Table 5.2.

A compilation of reconstruction resolution results from the various methods used is given in Table 5.2. In each case the value of the error parameter bracketing 50% and 90% of the distribution is given. Given the similarity of geometrical reconstruction for Methods 2 and 3, the energy and depth of maximum resolution is given for Method 2 only. Method 0 represents the reconstruction with fluorescence data alone. Some of these data are displayed graphically in Figure 5.27.

	10^{19} eV		10^{20} eV	
	Surface	Hybrid	Surface	Hybrid
$\Delta\theta$	$2.0°$	$0.35°$	$1.0°$	$0.36°$
Δcore	80 m	29 m	40 m	29 m
$\Delta E/E$	18%	4.2%	7%	2.5%
ΔX_{max}		17 g/cm^2		15 g/cm^2

Table 5.3: Summary and comparison of reconstruction resolution for the surface array alone and for Hybrid data. Median errors are shown, from simulations of proton showers.

5.4 Summary of Reconstruction Resolution

Simulations of the surface array performance predict that the reference design will provide data which can be used to reconstruct the energy, direction, and nuclear composition of the highest energy cosmic rays. The resolution of the reconstructions is more than sufficient to interpret the data in the context of the scientific models described in Chapter 2.

The hybrid data set – those events which have been simultaneously recorded by the surface array and one or more of the fluorescence detector "eyes"– will yield a subset of events which are particularly well measured, having independent data on energy and direction. The hybrid data set reconstructions are significantly improved over that of the surface array alone. When coupled with determination of X_{max}, these will greatly enhance the analysis of cosmic ray composition.

Table 5.3 summarizes the median reconstruction errors for various quantities. The values shown display the resolution expected from analysis of surface data alone, and the improvement expected for hybrid events. This brief summary gives representative values, obtained from the tabulations and detailed summaries found earlier in this chapter (e.g., Figure 5.15 and Table 5.2).

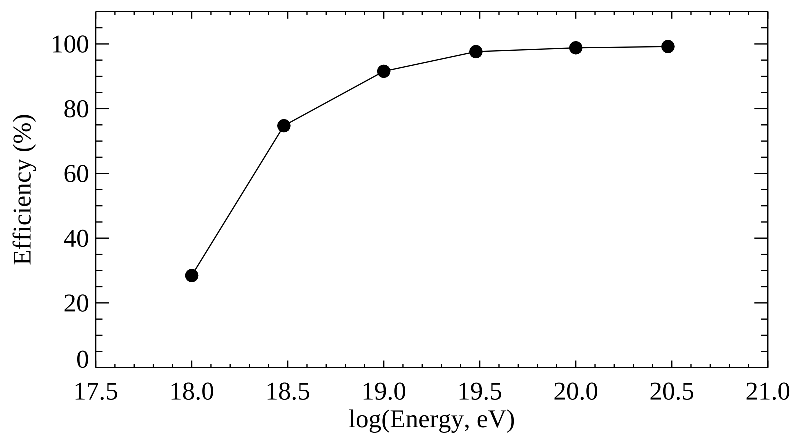

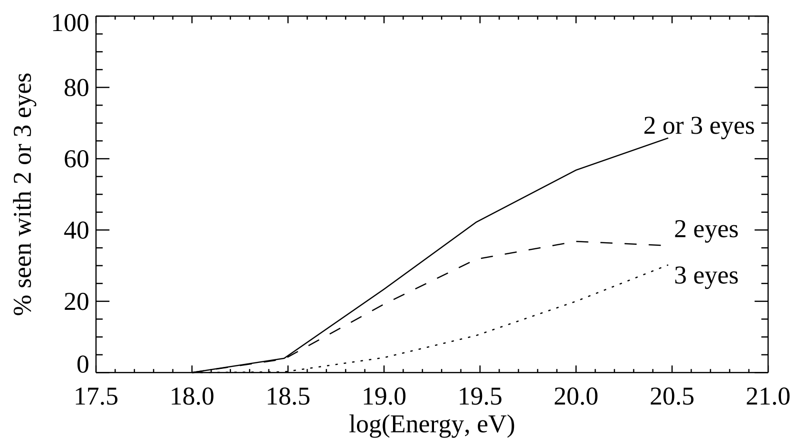

Figure 5.19: (a) Triggering/reconstruction efficiency as a function of primary energy. Showers were restricted to zenith angles less than 60° and cores within the 3000 km^2 area of the array. At least one of the eyes must have triggered in coincidence with the ground array. The fraction of triggering showers successfully passing through the reconstruction process has been included in the efficiency. (b) The fraction of showers triggering the array and exactly 2 eyes, exactly 3 eyes, and 2 or 3 eyes.

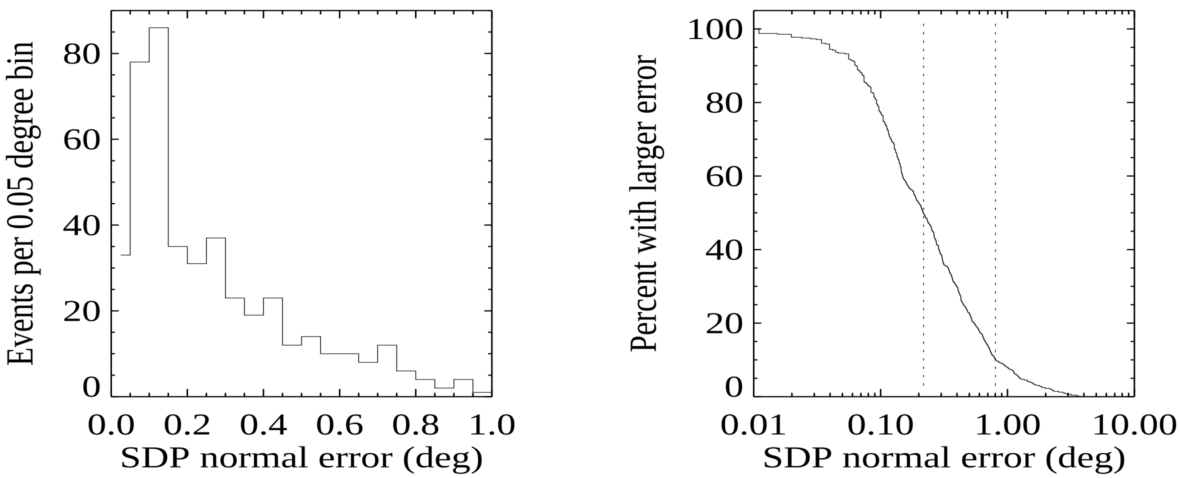

Figure 5.20: The error distribution for the *normal* to the shower-detector plane (SDP), for all showers triggering the Hybrid detector at 10^{19}eV. The differential and integral forms of the error distribution are shown. It can be seen that 50% of the plane normal errors are smaller than 0.22° and 90% are smaller than 0.80°.

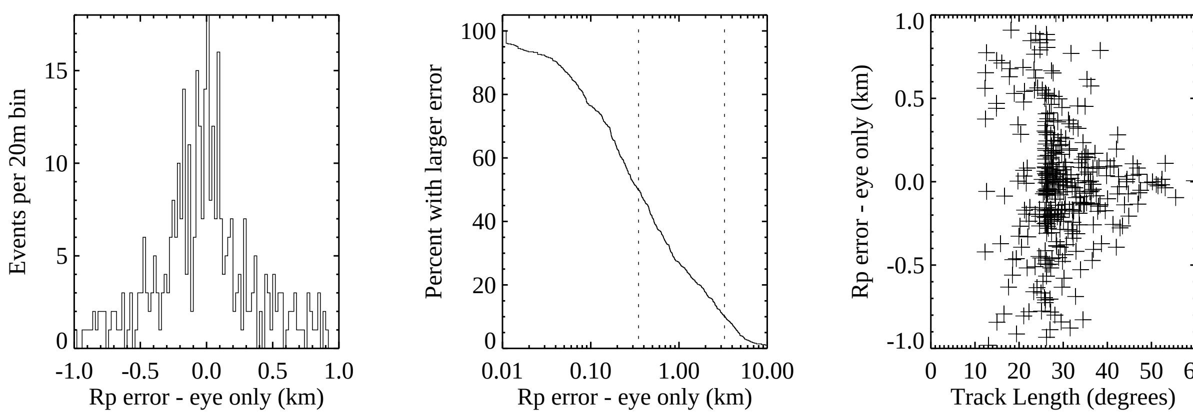

Figure 5.21: Reconstruction errors for the impact parameter R_p (see Figure 5.18). The resolution in this measurement (and that of the ground angle ψ) is strongly dependent on the length of the shower track viewed by the eye. Results shown for 10^{19}eV showers triggering the Hybrid array. Only fluorescence information is used in the reconstruction here.

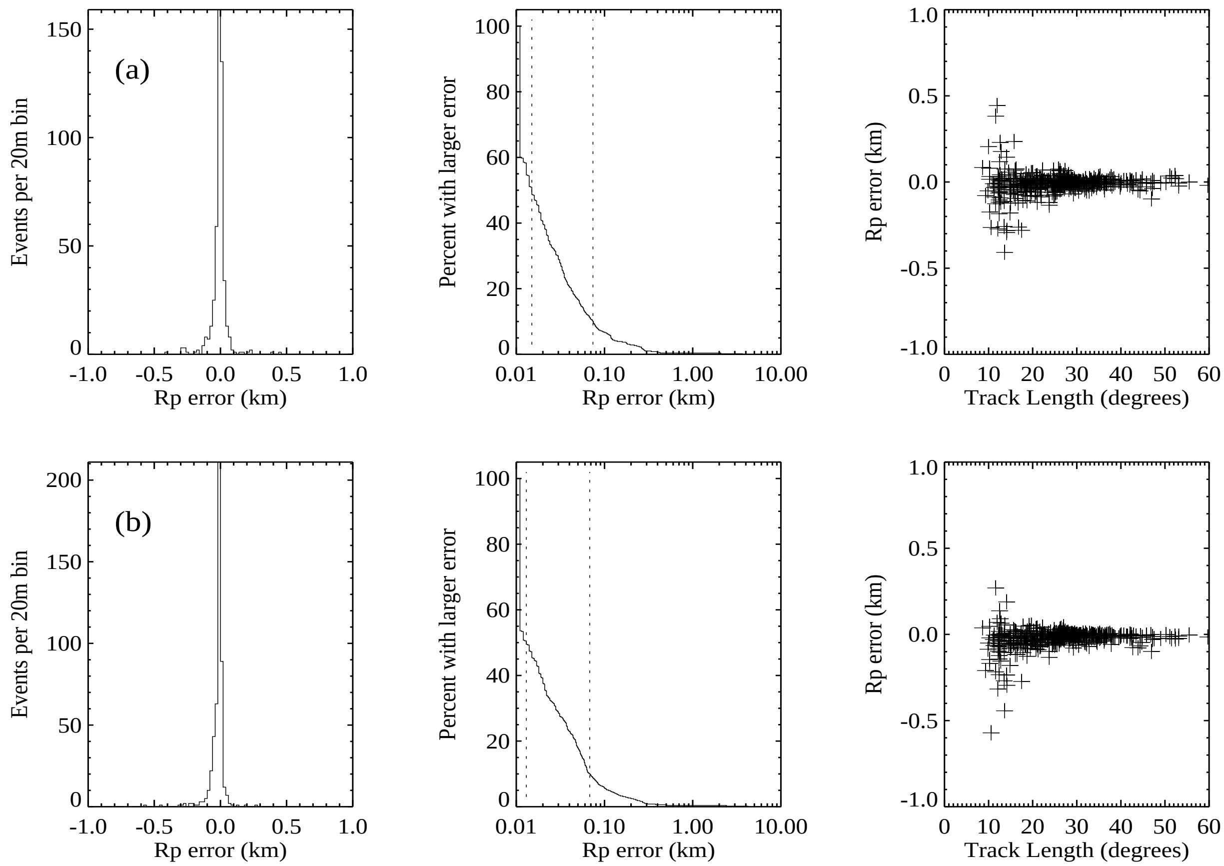

Figure 5.22: Impact parameter error distributions for (a) Method 2 and (b) Method 3 on 10^{19}eV triggered showers. The track length dependence of the error has dramatically lessened.

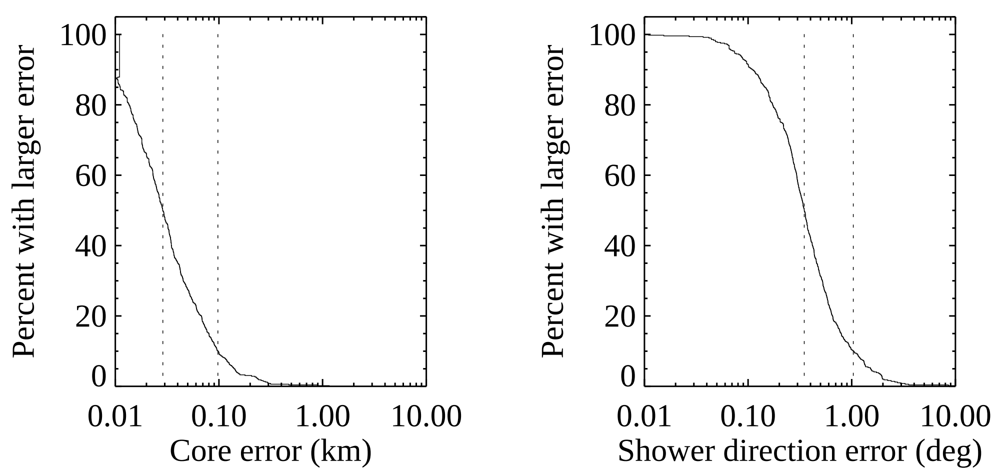

Figure 5.23: The final core location and shower direction errors for showers at 10^{19}eV analysed with Method 2.

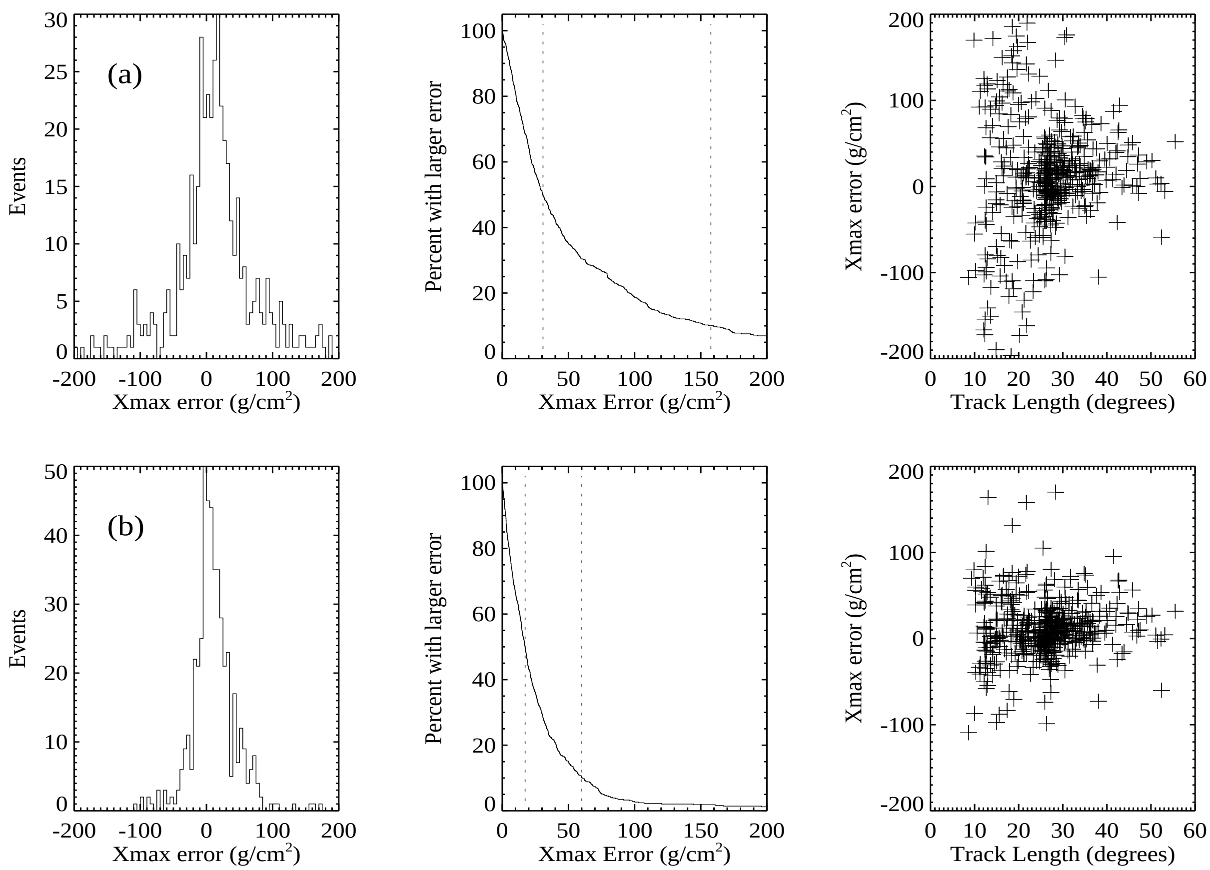

Figure 5.24: Profile reconstruction for 10^{19}eV showers. All showers triggering the Hybrid array have been included here. In (a) is shown the X_{max} error ($Xmax_{reconstructed} - Xmax_{true}$) for showers analysed using the fluorescence information alone. In (b) are shown the same showers analysed using Hybrid Method 2.

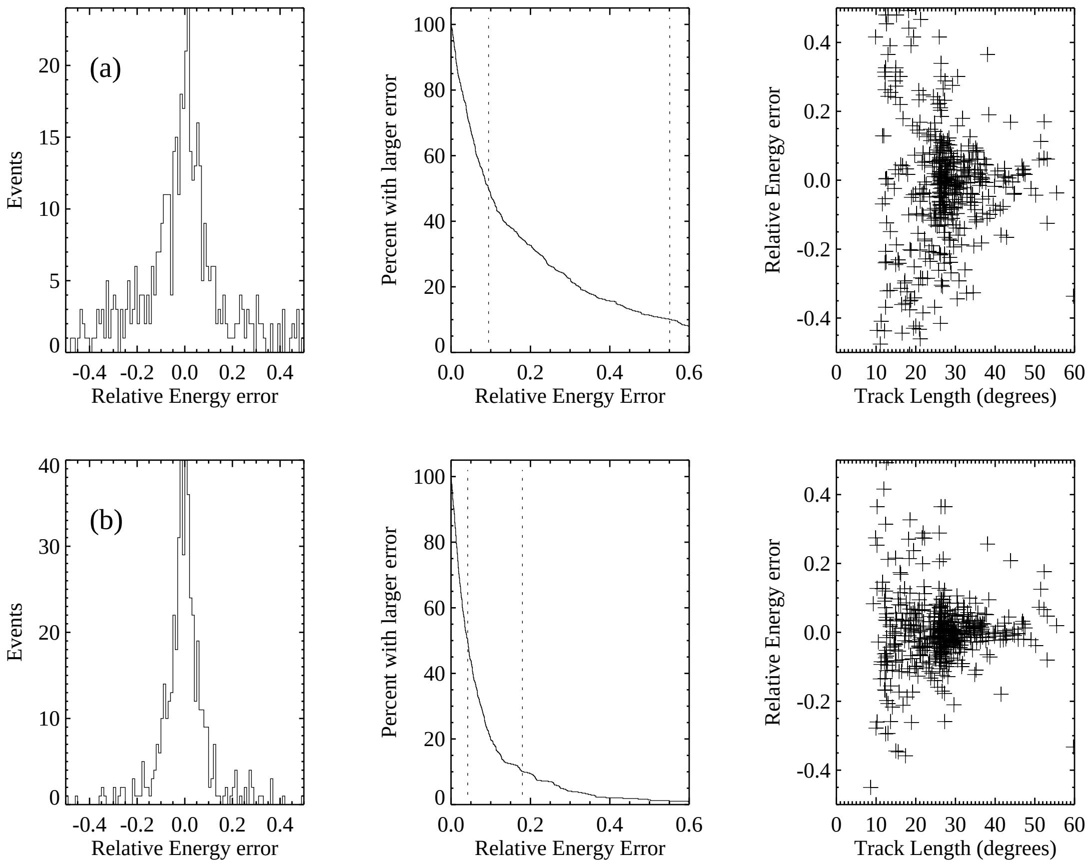

Figure 5.25: Energy resolution $(E_{reconstructed} - E_{true})/E_{true}$ for 10^{19}eV showers analysed with data from (a) the fluorescence detector only, and (b) with Hybrid data using Method 2.

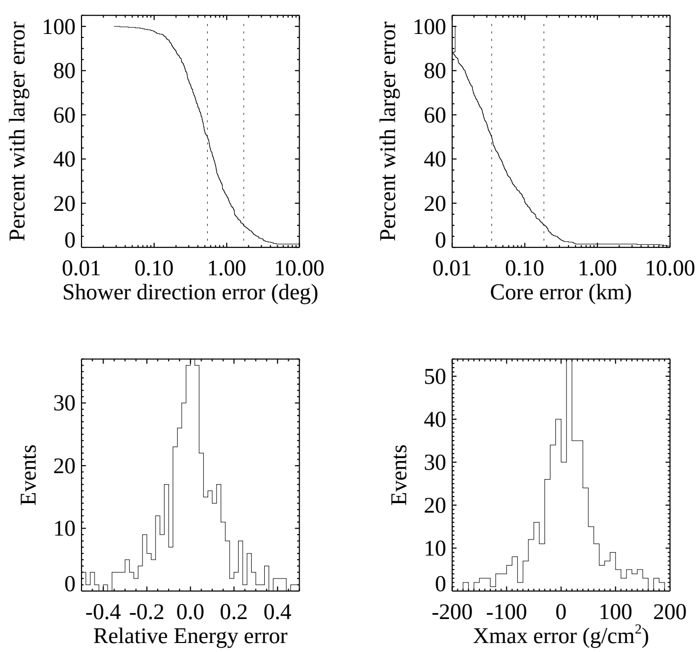

Figure 5.26: Reconstruction of lower energy (10^{18}eV) showers using Method 2.

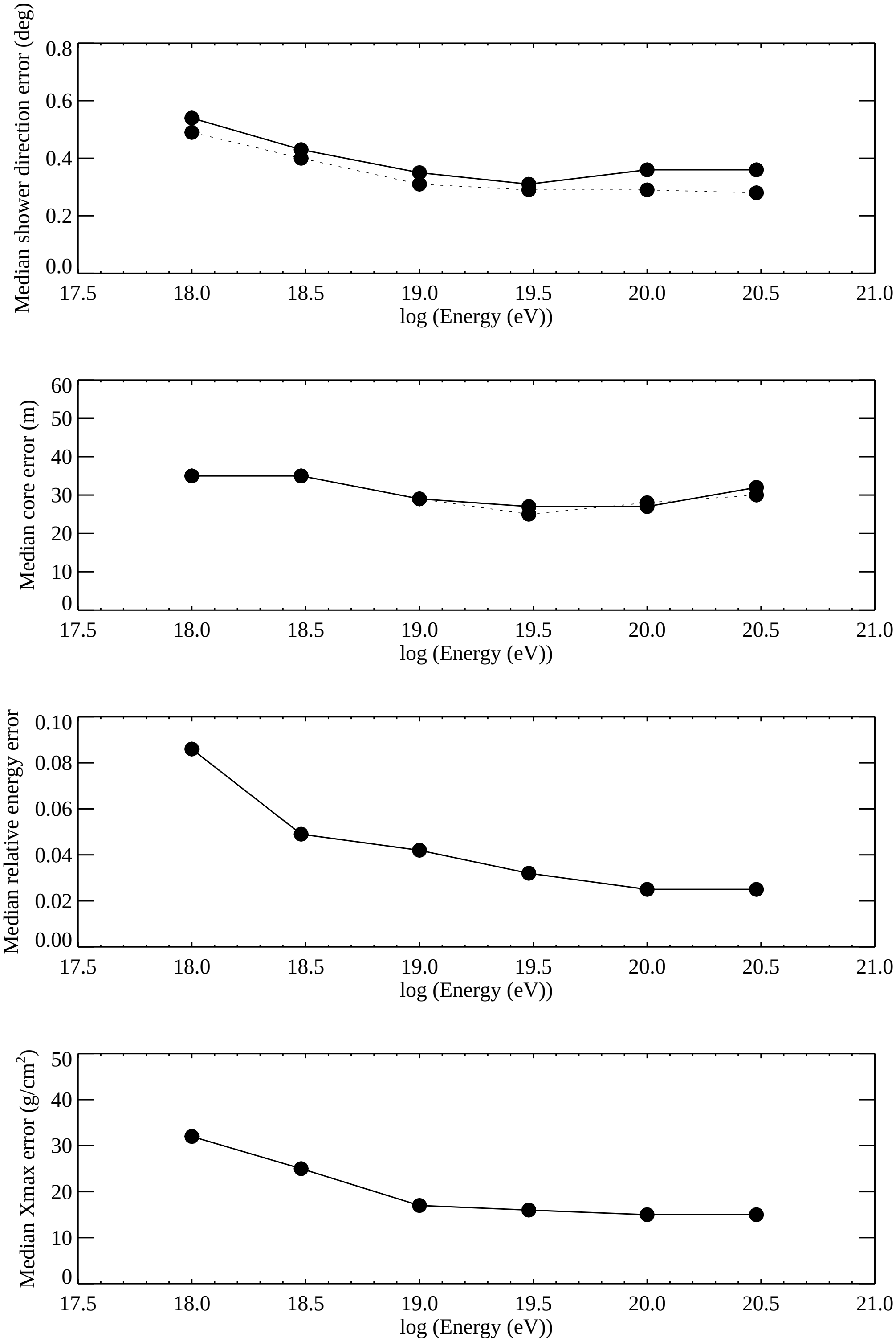

Figure 5.27: Hybrid median reconstruction errors for the three eye, 1.5° pixel system. The errors for the geometical quantities (shower direction and core) are shown for Methods 2 (solid line) and 3 (dashed line), though the errors are almost identical. The energy and $X_{\max}$ errors are shown for Method 2. A summary of these data, together with 90% errors, is given in Table 5.2.